澳門大學
UNIVERSIDADE DE MACAU
UNIVERSITY OF MACAU

Outstanding Academic Papers by Students
學生優秀作品

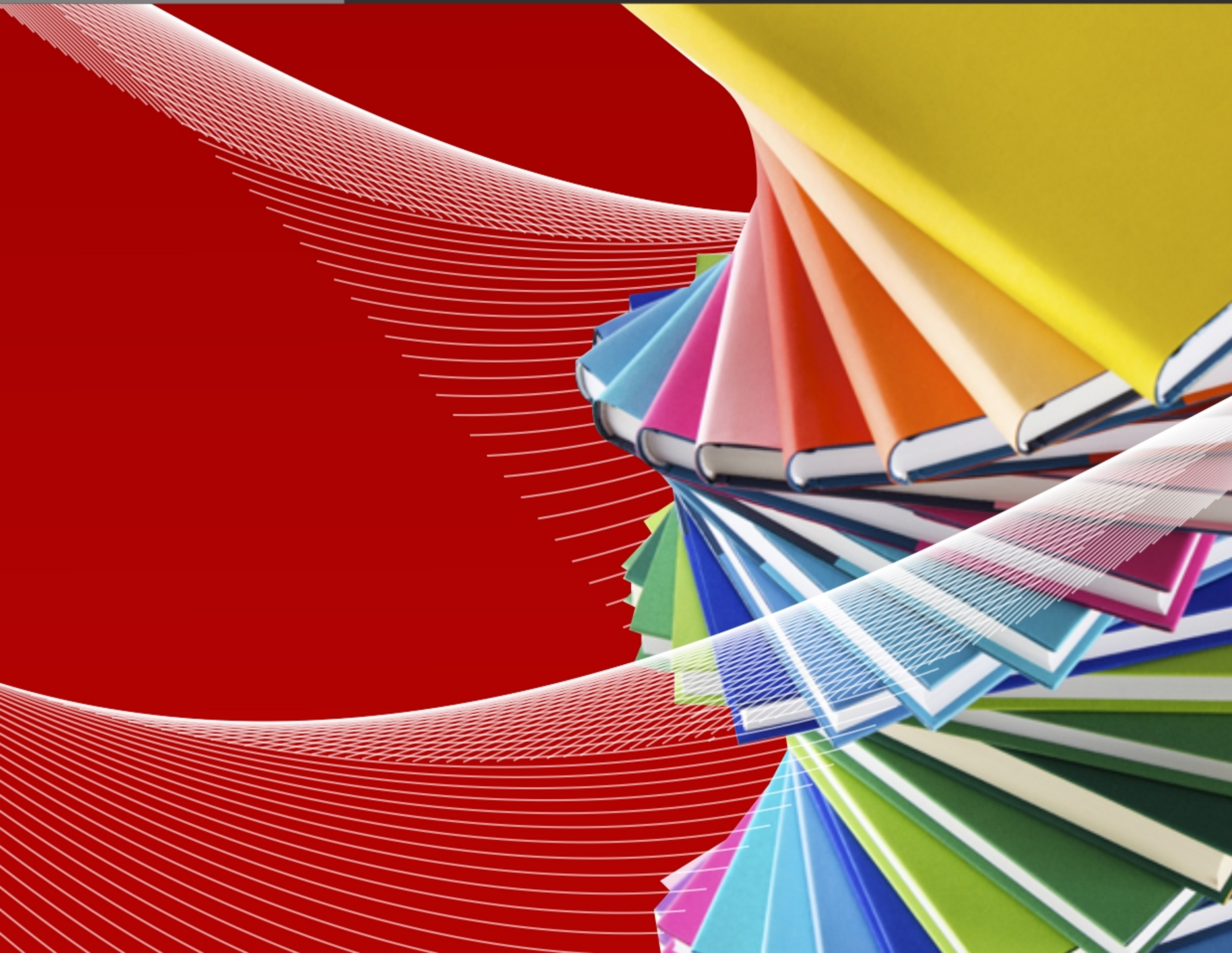

DESIGN AND CONTROL OF A MICRO-SYRINGE PUMP DRIVEN BY PIEZOELECTRIC ACTUATOR

by

Wen Shihao (D-B2-2739-2)

Lei In Nam (D-B2-2740-4)

Wu Zeyi (D-B2-2826-9)

B.Sc. in Electromechanical Engineering

2015/2016

Faculty of Science and Technology
University of Macau

Design and control of a micro-syringe pump driven by piezoelectric actuator

by

Wen Shihao (D-B2-2739-2)

Lei In Nam (D-B2-2740-4)

Wu Zeyi (D-B2-2826-9)

Final Year Project Report submitted in partial fulfillment of the requirements for the degree of

B.Sc. in Electromechanical Engineering

Faculty of Science and Technology
University of Macau

2015/2016

University of Macau

Abstract

DESIGN AND CONTROL OF A MICRO-SYRINGE PUMP DRIVEN BY PIEZOELECTRIC ACTUATOR

by Wen Shihao (D-B2-2739-2)

Lei In Nam (D-B2-2740-4)

Wu Zeyi (D-B2-2826-9)

Project Supervisor
Prof. Xu Qingsong

In this project, the design and testing of a micro-syringe pump is conducted for precision delivery of liquid inside a tube. A single-axis micro-motion pump is designed by using flexure mechanisms for precision drive of the micro-syringe. Based on the specifications on travel range and load capability, a translational motion mechanism is developed. The machine parameters are designed and optimized to cater for the requirement on pump performance. The performance is verified by conducting finite element analysis simulations. A prototype pump actuated by a piezoelectric actuator is developed, a feedback controller is designed, and experiment studies are conducted for precision pump testing under a microscope.

TABLE OF CONTENTS

LIST OF FIGURES i
LIST OF TABLES iv
LIST OF ABBREVIATIONS v
ACKNOWLEDGMENTS vi
CHAPTER 1: INTRODUCTION 1
    1.1. BACKGROUND 1
    1.2. VARIOUS SYRINGE PUMP DRIVERS 1
    1.3. OBJECTIVE 2
CHAPTER 2: MAIN MECHANISM AND FIXTURE DESIGN 4
    2.1. AMPLIFIER 4
        2.1.1. MAGNIFICATION CALCULATION 4
        2.1.2. DESIGN VARIABLES OF AMPLIFIER 5
    2.2. COMPOUND PARALLELOGRAM FLEXURES 6
        2.2.1. INTRODUCTION OF COMPOUND PARALLELOGRAM FLEXURES 6
        2.2.2. TWO DESIGNS AND THE SELECTION 7
    2.3. COMPONENT FIXTURES 8
CHAPTER 3: OPTIMIZATION AND SIMULATION 9
    3.1. OPTIMIZATION CONSTRAINTS 9
    3.2. OPTIMIZATION RESULTS 10
    3.3. SIMULATION RESULTS 12
    3.4. ASSEMBLY MODEL 15
CHAPTER 4: PROTOTYPE FABRICATION AND ASSEMBLY 16
CHAPTER 5: EXPERIMENTS AND DATA PROCESSING 18
    5.1. LABVIEW PROGRAM DEVELOPMENT 18
    5.2. GAINS TUNING FOR CONTROLLER 19
    5.3. EQUIPMENT PERFORMANCE 20
        5.3.1. OPEN-LOOP TEST 20
        5.3.2. CLOSE-LOOP TEST 20

5.4. SYRINGE OUTPUT DATA PROCESSING 24
5.4.1. LIQUID LEVEL IDENTIFICATION 24
5.4.2. SYRINGE OUTPUT 25
CHAPTER 6: DISCUSSION 28
CHAPTER 7: CONCLUSION 30
REFERENCES 31
APPENDIX A: MODEL ANALYSIS RESULTS 33
APPENDIX B: CAD DRAWINGS FOR THE MICRO-SYRINGE PUMP 34
APPENDIX C: COMPONENTS LIST OF THE MICRO-SYRINGE PUMP 44
APPENDIX D: DEVICES USED IN EXPERIMENT 50
APPENDIX E: PUBLICATION 51
APPENDIX F: WORK BREAKDOWN 52

LIST OF FIGURES

Number *Page*

Figure 1: A flexure-based bridge-type displacement amplifier with a backward output 4

Figure 2: One quarter of the compound bridge-type amplifier and its parameters 4

Figure 3: (a), (b) Two different CPFs unit..6

Figure 4: (a) Deformation of a CPF, (b) Dimensions of one flexure and (c) Cross-section 6

Figure 5: (a) First design and (b) second design, both with an amplifier...........................7

Figure 6: The CAD model of syringe fixtures...8

Figure 7: The CAD model of sensor fixtures 8

Figure 8: The top view of main structure after optimization..12

Figure 9: (a) The two displacement inputs, (b) the target of output displacement measurement 13

Figure 10: The safety factor simulation result...13

Figure 11: (a) The two force inputs, (b) the target of thrust surface displacement measurement 14

Figure 12: The first mode of the structure...15

Figure 13: (a), (b) the assembly models 15

Figure 14: The physical assembly of the micro-syringe pump...16

Figure 15: The experimental setup of the system...17

Figure 16: The block diagram of experimental setup...17

Figure 17: The block diagram (some of the cases are not be shown)...............................18

Figure 18: The control panel of the LabVIEW program includes sensor zeroing panel (in blue), parameter setting panel (in red) and graph panel (in green), and those parameters' value are not the final set...19

Figure 19: The output under a 1-V input...20

Figure 20: The relationship between the displacement and the voltage...........................21

Figure 21: (a) The voltage change (in green) during the process; (b) The error (in magenta) during the process; (c) The output (in red) and setpoint (in blue) ...21

Figure 22: Under a 0.5-Hz sinusoidal signal: (a) The output (in red) and setpoint (in blue); (b) The error (in magenta) during the process; (c) The voltage change (in green) during the process; (d) The hysteresis loop (in black) 22
Figure 23: Under a 5-Hz sinusoidal signal: (a) The output (in red) and setpoint (in blue); (b) The error (in magenta) during the process; (c) The voltage change (in green) during the process; (d) The hysteresis loop (in black) 23
Figure 24: (a) The voltage change (in green) during the process; (b) The error (in magenta) during the process; (c) The output (in red) and setpoint (in blue) ...23
Figure 25: The microscope and the tube...24
Figure 26: The parameters when the liquid in a small tube..25
Figure 27: The processed picture. (a) The "valley"; (b) The "peak"; (c) The merged picture (d) The analysis to the merged picture 26
Figure 28: The first six resonant frequencies of the main structure 33
Figure 29: Amplifier...34
Figure 30: Amplifier Spacer 35
Figure 31: Base 36
Figure 32: CPF...36
Figure 33: CPF Spacer...37
Figure 34: L Shape Connector...38
Figure 35: Sensor Support Frame Pillar Long..38
Figure 36: Sensor Support Frame Pillar Short..39
Figure 37: Sensor Support Frame Bracket 40
Figure 38: Syringe Bracket..41
Figure 39: Syringe Outer Barrel Fixture Front...42
Figure 40: Syringe Outer Barrel Fixture Top 43
Figure 41: Syringe Push Rob Fixture 43
Figure 42: Amplifier...44
Figure 43: Amplifier Spacer 44
Figure 44: Base 45
Figure 45: CPF...45
Figure 46: CPF Spacer...45
Figure 47: L Shape Connector...46

Figure 48: Sensor Fixture 46
Figure 49: Sensor Support Frame Bracket 46
Figure 50: Sensor Support Frame Pillar Long..47
Figure 51: Sensor Support Frame Pillar Short..47
Figure 52: Syringe 47
Figure 53: Syringe Bracket..48
Figure 54: Syringe Outer Barrel Fixture Front...48
Figure 55: Syringe Outer Barrel Fixture Top 48
Figure 56: Syringe Push Rob Fixture 49
Figure 57: Screws, nuts and washers...49
Figure 58: Piezoelectric Actuator...49

LIST OF TABLES

Number *Page*
Table 1: The constraints of the main structure’s performances 9
Table 2: The constraints of the main structure’s design variables 10
Table 3: The optimization results of two thicknesses 11
Table 4: The mechanical properties of Al-7075 12
Table 5: The gains of PID controller 20
Table 6: The data by pictures analyzing 26

LIST OF ABBREVIATIONS

PEA. Piezoelectric Actuator

CPF. Compound Parallelogram Flexure

PID. Proportional–Integral–Derivative

CBT. Compound Bridge-Type

CAD. Computer-Aided Design

PMMA. Polymethyl Methacrylate

DAC. Digital to Analog Converter

ACKNOWLEDGMENTS

The authors would like to express their gratitude to Prof. Xu Qingsong, for his professional guidance, patient instruction and kind support to complete this project, and to the graduate students of the Smart and Micro/Nano Systems Laboratory for their assistance with experiment setup and valuable advices in this project.

CHAPTER 1: INTRODUCTION

1.1. BACKGROUND

Over the past few years, a considerable number of studies have been made on syringe pump systems which have been widely applied and rapidly expanded to a variety of fields [1]. Common applications include chemical analysis [2], drug delivery [3-5], single cell manipulation analysis and DNA analysis [6].

The major component of the syringe pump systems is the syringe which is widely used in the medical field for long-term constant injection of drugs [7]. Conventional syringe pumps consist of hand driven motion of the plunger, which is not adapted for precision delivery of liquid [8]. Therefore, automated syringe pump systems are required to deal with this issue.

1.2. VARIOUS SYRINGE PUMP DRIVERS

So far, many available applications have been developed [9, 10]. There are some common applications with different syringe pump drivers.

The typical mechanical syringe pump system used an endless worm thread to put the syringe plunger in motion. The circular movement of stepping motor operated the endless thread. Also, a spring was used to push the plunger in order to maintain a constant force [11]. The syringe pump system was suitable due to a large range of liquid flow. The weakness of the system is its complexity which can easily lead to operational error. In addition, minimizing the start-up delays is also a challenge. On the other hand, oscillations or pulse phenomena appear at low flow rate for most syringe pumps driven by the motor as volume injected in the tubing and movement of the piston are correlated.

SQUIGGLE syringe pump driven by SQUIGGLE motors was designed in very small dimensions and directly connected to the syringe [12]. The motor directly rotated a screw by using ultrasonic standing wave vibrations in a threaded nut. It was dramatically small and provided quiet operation, no pressure pulses, much great output pressure and flow.

However, the power and precision of the SQUIGGLE motors cannot be matched by traditional electric syringe pump. The smaller size of motor require operation at higher speeds which causes even lower efficiency and reduced accuracy.

Moreover, with the development of microfluidic devices, microfluidic systems for manipulating cell have been explored. Therefore, the syringe pump systems with PEA have been used in related areas [13]. However, the backlash problem due to plunger motion appeared which was caused by the mechanical hysteresis of pump mechanism.

1.3. OBJECTIVE

Since each syringe pump system has specific strengths and weaknesses, there is a clear need for a simple, compact, and easy-to-use syringe driver, which is developed in this project. In comparison to current mechanical method [14], piezoelectric actuator (PEA) based on the piezoelectric effect of piezoelectric ceramics [15, 16] has many attractive features. For example, PEA delivers large force, fast response, and high energy conversion efficiency [17]. It can solve most problems occurred in pervious syringe pump system. Therefore, PEA is applied in this project. Moreover, in order to deal with the backlash problem which cannot obtain continuous and sufficiently stable output [18], the conceptual design of a micro-syringe pump with flexure structure is proposed in this work to overcome the current issue.

The equipment is composed of a PEA, a displacement amplifier, a compound parallelogram flexure (CPF) structure, some fixtures for the components, and a syringe connected to the tube. In this project, in order to achieve convenient testing and high speed response, PEA and capacitance sensor are employed as actuator and displacement sensor, respectively. To achieve the required performance and to limit the physical size of equipment, finite element analysis (FEA) and parameter optimization are carried out in the design process. For the practical application of micro-syringe pump, proportional–integral–derivative (PID) control is realized in the control process. The outlet of the syringe is connected with a tube, and the result is monitored under a microscope. Through the experimental study, the complete micro-syringe pump device is characterized to verify the proposed design.

CHAPTER 2: MAIN MECHANISM AND FIXTURE DESIGN

2.1. AMPLIFIER

In order to solve the small travel stroke problem of PEAs, a mechanical displacement amplifier is used to amplify the stroke in order to achieve large output displacements [19].

2.1.1. MAGNIFICATION CALCULATION

The analytical modelling of a compound bridge-type (CBT) compliant displacement amplifier has developed in the previous work [20]. It derives simple and reliable expressions of the amplification ratio, which is helpful to the design process.

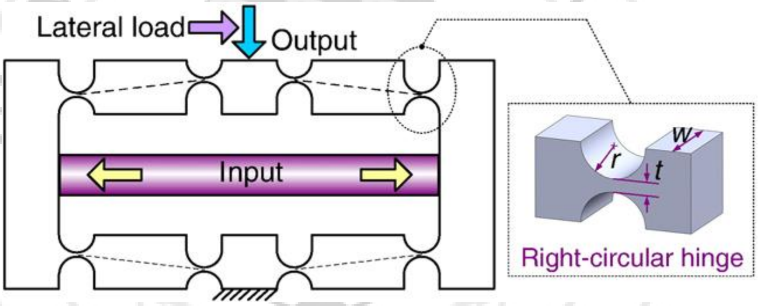

Figure 1: A flexure-based bridge-type displacement amplifier with a backward output

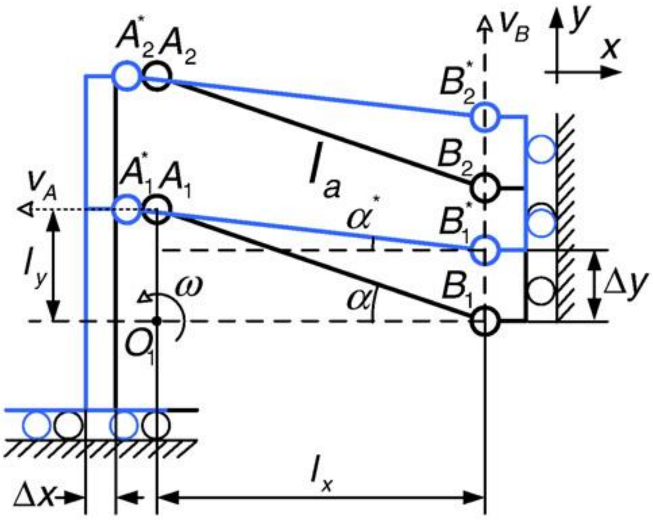

Figure 2: One quarter of the compound bridge-type amplifier and its parameters

Assume that each of the flexure hinge has a 1-DOF rotational compliance, which arises from the rotational deformation, and others are rigid bodies. The one quarter model of the amplifier is shown in Figure 2.

Referring to Figure 2, the horizontal input displacement $\mathit{\Delta} x$ produces a vertical output displacement $\mathit{\Delta} y$, which reduces the incline angle of A_1B_1 (A_2B_2) from α to α^*. In view of the projection of A_1B_1 (A_2B_2) in the x- and y-axes directions, there comes the following relations:

$$l_a cos\alpha + \mathit{\Delta} x = l_a cos\alpha^*, \tag{1}$$

$$l_a sin\alpha - \mathit{\Delta} y = l_a sin\alpha^*, \tag{2}$$

where l_a denotes the length of A_1B_1 (A_2B_2).

Variable α^* can be eliminated by adding the squares of Eq. (1) and (2), i.e.,

$$\mathit{\Delta} y^2 - 2l_a sin\alpha \mathit{\Delta} y + \mathit{\Delta} x^2 + 2l_a cos\alpha \mathit{\Delta} x = 0, \tag{3}$$

which allows the generation of an expression for the output displacement:

$$\mathit{\Delta} y = l_a sin\alpha - \sqrt{l_a^2 sin^2\alpha - \mathit{\Delta} x^2 - 2l_a cos\alpha \mathit{\Delta} x}, \tag{4}$$

where the other solution with the "+" sign before the root is discarded because its value is too large that cannot be achieved in practice.

Therefore, the amplification ratio of the CBT amplifier can be derived as:

$$A = \frac{\mathit{\Delta} y}{\mathit{\Delta} x} = \frac{l_a sin\alpha - \sqrt{l_a^2 sin^2\alpha - \mathit{\Delta} x^2 - 2l_a cos\alpha \mathit{\Delta} x}}{\mathit{\Delta} x}. \tag{5}$$

2.1.2. DESIGN VARIABLES OF AMPLIFIER

According to Eq. (5), when $\mathit{\Delta} x$ is known, it's easy to find that the amplification ratio is only relaying to l_a and α:

$$A(\, l_a, \alpha). \tag{6}$$

However, l_a and α is hard to mark down in the model sketch when building a CAD model, so it needs to be simplified. Referring to Figure 1, the length of l_a and the angle α relay to the radius of hinge r, the thickness of hinge t, the block length $l_{block-x}$ and the block width $l_{block-y}$, then Eq. (6) becomes:

$$A(r, t, l_{block-x}, l_{block-y}). \tag{7}$$

According to the above relationship, there are only four simple design variables are considered in optimizing process:

$$Amplifier(r, t, l_{block-x}, l_{block-y}). \tag{8}$$

2.2. COMPOUND PARALLELOGRAM FLEXURES

2.2.1. INTRODUCTION OF COMPOUND PARALLELOGRAM FLEXURES

A flexure-based compliant structure delivers motion by making use of elastic deformations of the material, which allows the generation of a smooth output motion by eliminating the adverse effects in terms of clearance and backlash [21].

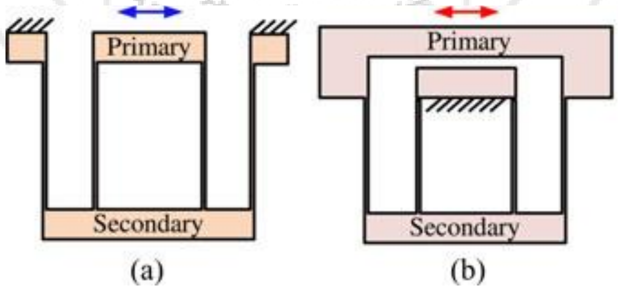

Figure 3: (a), (b) Two different CPFs unit

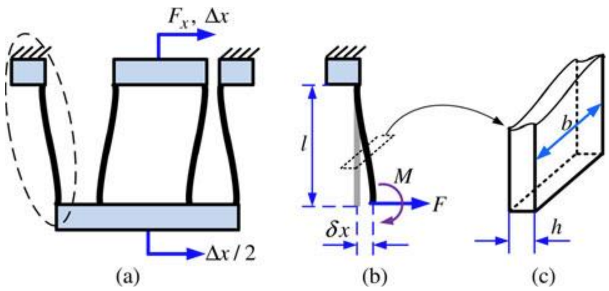

Figure 4: (a) Deformation of a CPF, (b) Dimensions of one flexure and (c) Cross-section

The CPFs as shown in Figure 3(a) and (b) have been widely used [22-25]. Referring to Figure 4, obviously the flexures play a key role in CPFs. Therefore, the length l, the width h and thickness b of flexures are three main design variables to affect the performance:

$$CPF(l, h\ , b). \tag{9}$$

In addition, the displacement is not very large for the micro-syringe pump (less than 1mm and close to 0.1mm), therefore, one pair of CPFs unit can be enough for smoothing output and also it is the main purpose to be used it in the design.

2.2.2. TWO DESIGNS AND THE SELECTION

Referring to Figure 3, there are two different kinds of CPFs which means there are two designs in this project. Figure 5(a) and (b) show the possible main mechanical designs.

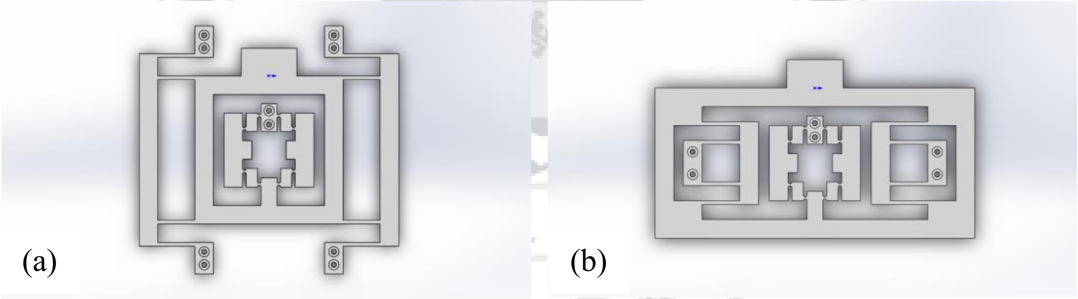

Figure 5: (a) First design and (b) second design, both with an amplifier

The selection are chosen by considering in the modifiability of design, the arrangement of other components and the weight. Since the second design is too wide to arrange other component and also heavier than the first design, the first design should be the best solution.

2.3. COMPONENT FIXTURES

A syringe is used in the equipment, hence, the fixtures of the syringe are also considered. Figure 6 shows the fixture of the syringe and the connector connecting the main structure and the syringe push rob.

Besides, a capacitive displacement sensor is used to determine the output of the main structure, the sensor is placed above the main structure and next to the connector, and the connector is also a sensing target. Figure 7 shows the fixture of the capacitive sensor.

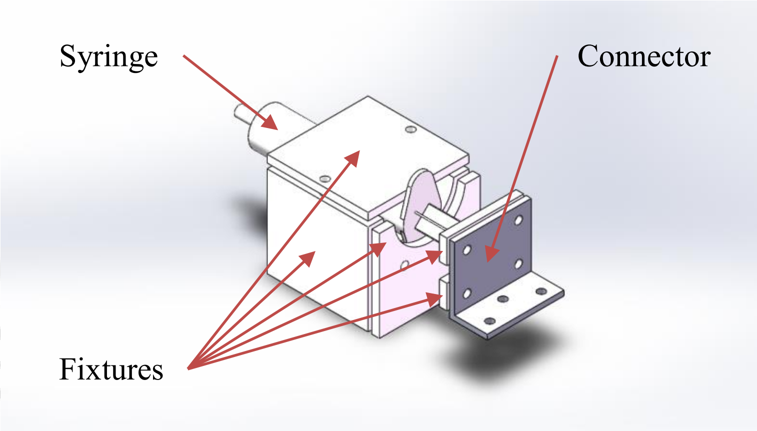

Figure 6: The CAD model of syringe fixtures

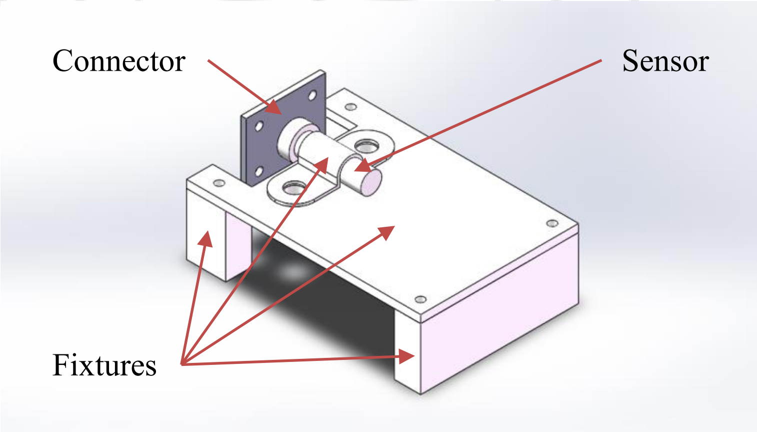

Figure 7: The CAD model of sensor fixtures

CHAPTER 3: OPTIMIZATION AND SIMULATION

3.1. OPTIMIZATION CONSTRAINTS

According to the idea of the dynamic characteristics of a structure, the output direction's natural frequency is an important indicator to indicate the performance of the structure. Therefore, the key point of optimization is to obtain a large enough natural frequency, also the input stiffness, output displacement and the safety factor are considered as constraints to satisfy the minimum requirement, the constraints are shown in Table 1.

Table 1: The constraints of the main structure's performances

	Constraint	Objective
Output Displacement	Greater than 7 times of input displacement	
Safety Factor	Inside Bounds [2, 5](mm)	
Input Stiffness	Less than actuator	
Natural Frequency	Greater than 100-Hz	Maximize

Then, referring to Eq. (8) and (9), the design variables of main structure can be summed up and express as:

$$Main\ Structure(r, t, l_{block-x}, l_{block-y}, l, h\ , b). \tag{10}$$

Due to the manufacturing convenience, the thickness h of the whole parts is chosen by past experience, that is 6-mm and 10-mm, then the variables are whittled down to a final six:

$$Main\ Structure(r, t, l_{block-x}, l_{block-y}, l, b). \tag{11}$$

To obtain a compact size of the main structure, the domain of these six variables should be reasonable ranges. Table 2 shows the ranges of each design variation:

Table 2: The constraints of the main structure's design variables

Design Variable	Domain(mm)
r	[0.5, 2.5]
t	[0.2, 1]
$l_{block-x}$	[10, 25]
$l_{block-y}$	[3, 15]
l	[10, 25]
b	[0.2, 1]

With this, it forms a single objective and multiple constraints problem.

3.2. OPTIMIZATION RESULTS

Since building a mathematic model with mechanical-related area needs a lot of derivation and calculation crossing over geometry and material mechanics, which is time-toke and difficult. By using the built-in optimization module in ANSYS Workbench, it does not need to prepare a mathematic model but the objective and constraints.

The adaptive single-objective (ASO) method is a gradient-based algorithm to provide a refined, global, optimization result [26]. To solve a single objective and multiple constraints problem, this method is used in optimize process.

The optimization module automatically chooses and ranks the best results. Table 3 shows the optimal results of two thicknesses:

Table 3: The optimization results of two thicknesses

Thickness	10-mm			6-mm		
Candidate Point	Point 1	Point 2	Point 3	Point 1	Point 2	Point 3
$l(mm)$	17.89	18.797	23.95	15.579	14.995	15.291
$b(mm)$	0.65854	0.68016	0.56	0.6513	0.64723	0.63414
$t(mm)$	0.52904	0.5558	0.352	0.452	0.43517	0.45303
$r(mm)$	1.0847	1.11395	1.28	0.92815	0.9789	0.96565
$l_{block-z}(mm)$	11.826	12.324	17.65	15.472	15.73	15.536
$l_{block-y}(mm)$	3.7624	3.8709	3.6	3.3698	3.481	3.6941
Output Displacement(μm)	101.98	102.37	195.69	103.45	102.33	105.49
Safety Factor	4.4558	4.5345	4.2515	4.8615	4.9697	4.9567
Input Stiffness ($kg/m^2 s^2$)	32258064.52	32739654.27	27687792.45	20218358.27	20403166.57	17198383.35
Natural Frequency (Hz)	242.96	240.24	105.48	221.56	220.59	217.64

For reference, the stiffness of the in-used PEA is 2.3×10^8-kg/m^{2}s^2, which is one order of magnitude larger than each result's input stiffness, and it should be mentioned that the material is Al-7075 in all the optimizing process. The mechanical properties of Al-7075 show in Table 4.

Table 4: The mechanical properties of Al-7075

Property	Value
Density	2810-kg m^3
Young’s Modulus	71.7-GPa
Poisson’s Ratio	0.33
Bulk Modulus	7.029-GPa
Shear Modulus	2.696-GPa
Tensile Yield Strength	503-MPa
Compressive Yield Strength	503-MPa
Tensile Ultimate Strength	572-MPa

By comparing the variable values of those two thickness, it is easy to make a choice since the point 1 of 10-mm thickness has the highest natural frequency, then this set of variable values is applied to design after taking two decimal places.

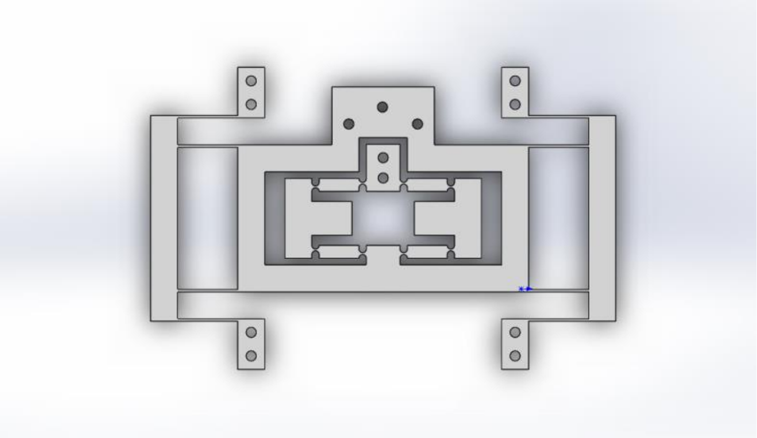

Figure 8: The top view of main structure after optimization

3.3. SIMULATION RESULTS

Before the manufacturing, a finite element analysis (FEA) should be finished for finding any potential mistake, since the parameter values were taken two decimal places.

Based on the static structural module in ANSYS Workbench, the simulation is starting by measure the maximum displacement. As shown in Figure 10 (a), the input displacement is 7.25-µm per side and the measurement target is the output of the whole structure. For reference, a total 14.5-µm displacement is just the maximum output of PEA.

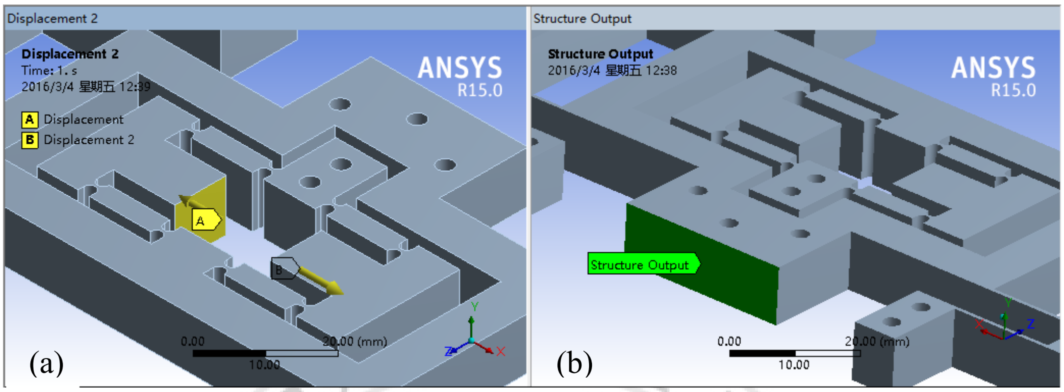

(a) (b)

Figure 9: (a) The two displacement inputs, (b) the target of output displacement measurement

The simulation result of the output displacement is 102.18-µm, it is larger than 7×14.5-µm=101.5-µm which fulfils the requirement. And with the input, the safety factor is 4.5017 which is also in the range.

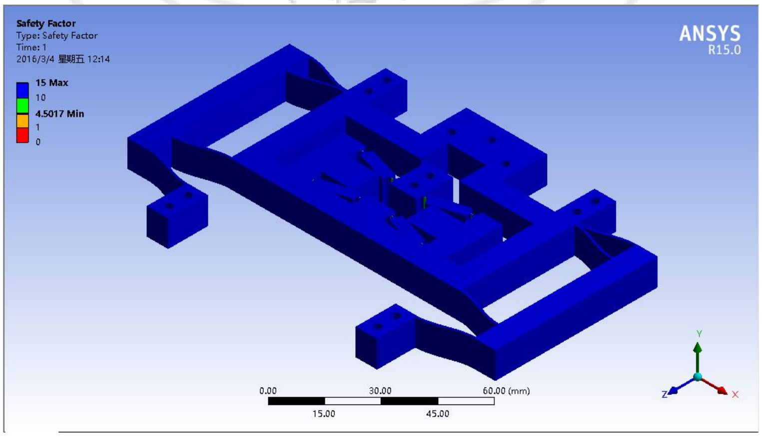

Figure 10: The safety factor simulation result

To calculate the input stiffness, it can be measured by applying a force to the input position and see the displacement of thrust surface, Eq. (12) shows the relationship of input stiffness, input force and the displacement:

$$Input\ stiffness = \frac{Input\ force}{Displacement\ of\ thrust\ surface}. \qquad (12)$$

In the simulation, 1-N force is applied to each side of input ends of amplifier as shown in Figure 11(a):

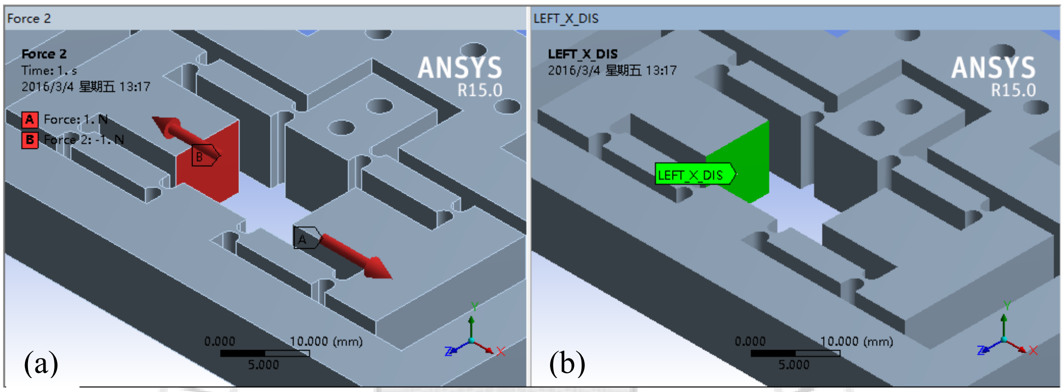

Figure 11: (a) The two force inputs, (b) the target of thrust surface displacement measurement

The simulation gives a result of 3.0385e-005 mm, so referring to Eq. (12), the input stiffness should be around 3.29×10^7-kg/m^{2}s^2, which is less than the stiffness of PEA (2.3×10^8-kg/m^{2}s^2). That means the actuator can easily drive the structure.

To measure the natural frequency, the modal analysis module was used. Figure 12 shows the first mode of the structure, and also shows the natural frequency of output direction which is 240.57-Hz: (For more detailed results about this simulation, please refer to Appendix A.)

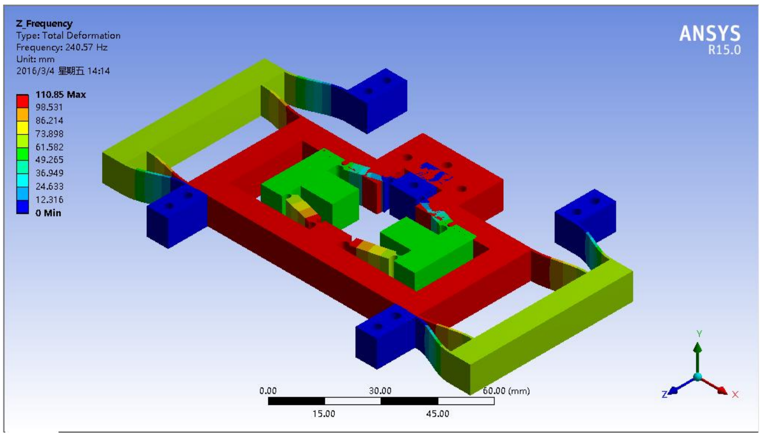

Figure 12: The first mode of the structure

3.4. ASSEMBLY MODEL

After the optimization and simulation processes to the main structure, all the CAD models' sizes can be confirmed and assembled for finding potential mistakes. Figure 13(a), (b) show two views of the assembly models.

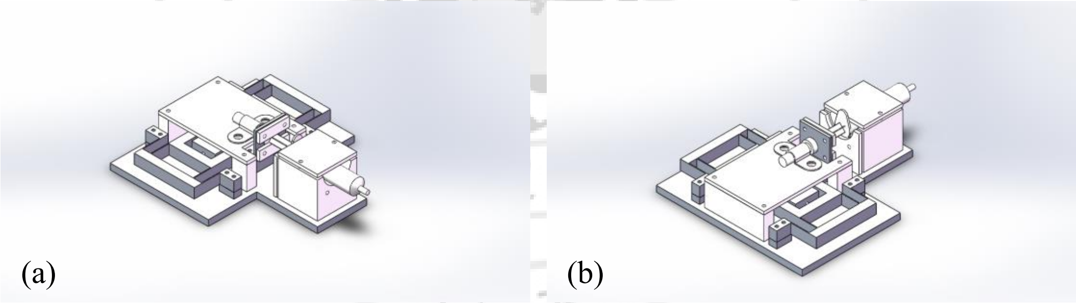

Figure 13: (a), (b) the assembly models

CHAPTER 4: PROTOTYPE FABRICATION AND ASSEMBLY

Based on the CAD models, the main structure was manufactured from Al-7075 in 0.01-mm tolerance, which had mentioned in the previous Chapter. Moreover, in order to reduce the manufacturing costs and total weight of structure, the fixtures of sensor and syringe was manufactured from polymethyl methacrylate (PMMA) in 0.1-mm tolerance, which under the condition of not affecting the output to guarantee compact and functional design. (Please refer to Appendix B to have more information of components.) Figure 14 shows the physical assembly of the micro-syringe pump, Figure 15 shows the experimental setup of the system and Figure 16 shows the idea of the experimental setup. (Please refer to Appendix C to see the components list of the micro-syringe pump)

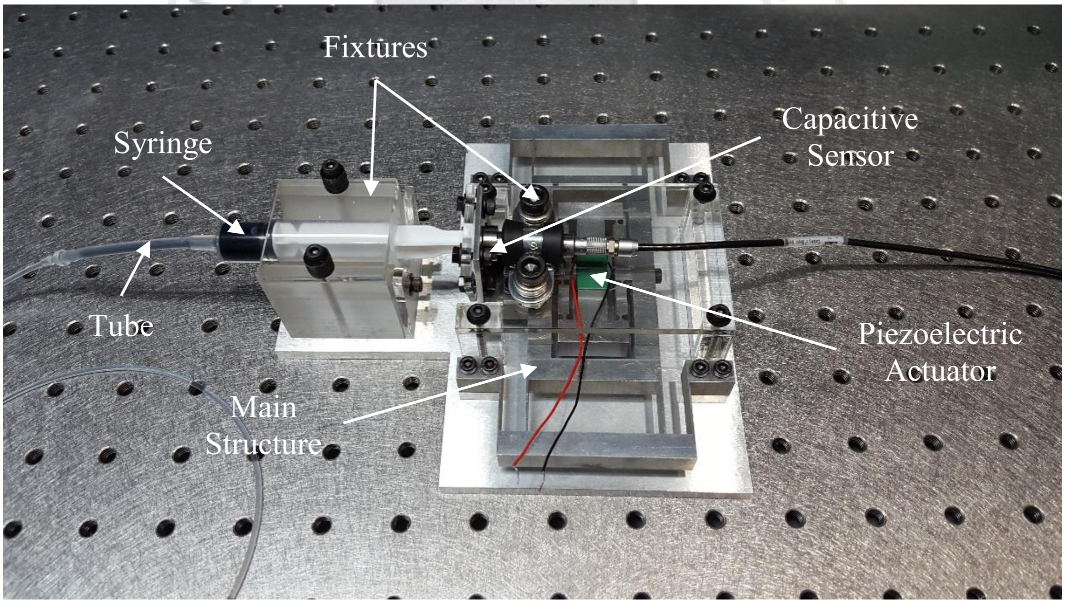

Figure 14: The physical assembly of the micro-syringe pump

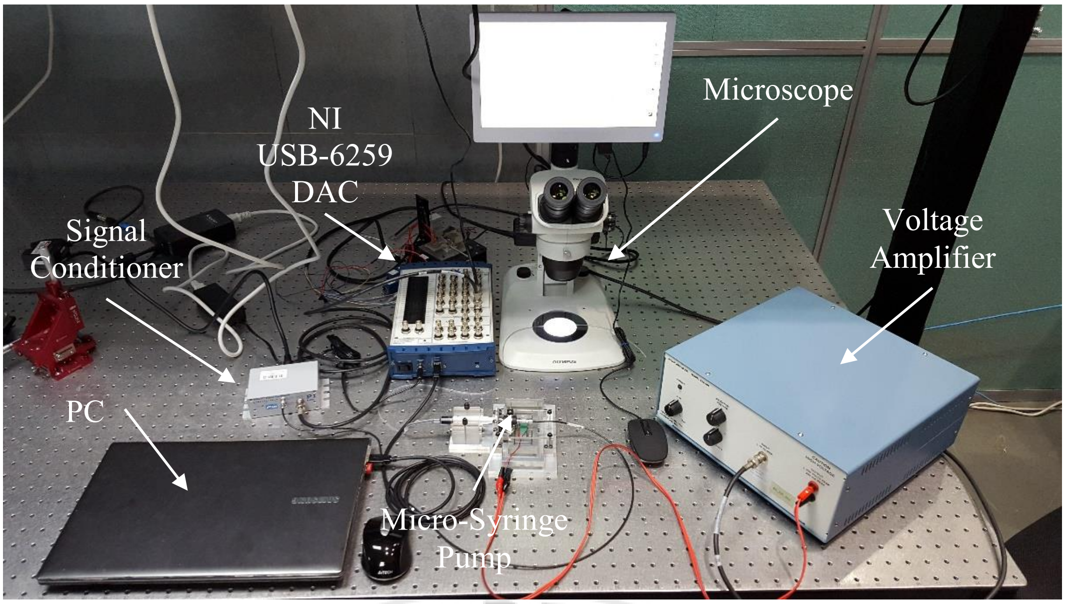

Figure 15: The experimental setup of the system

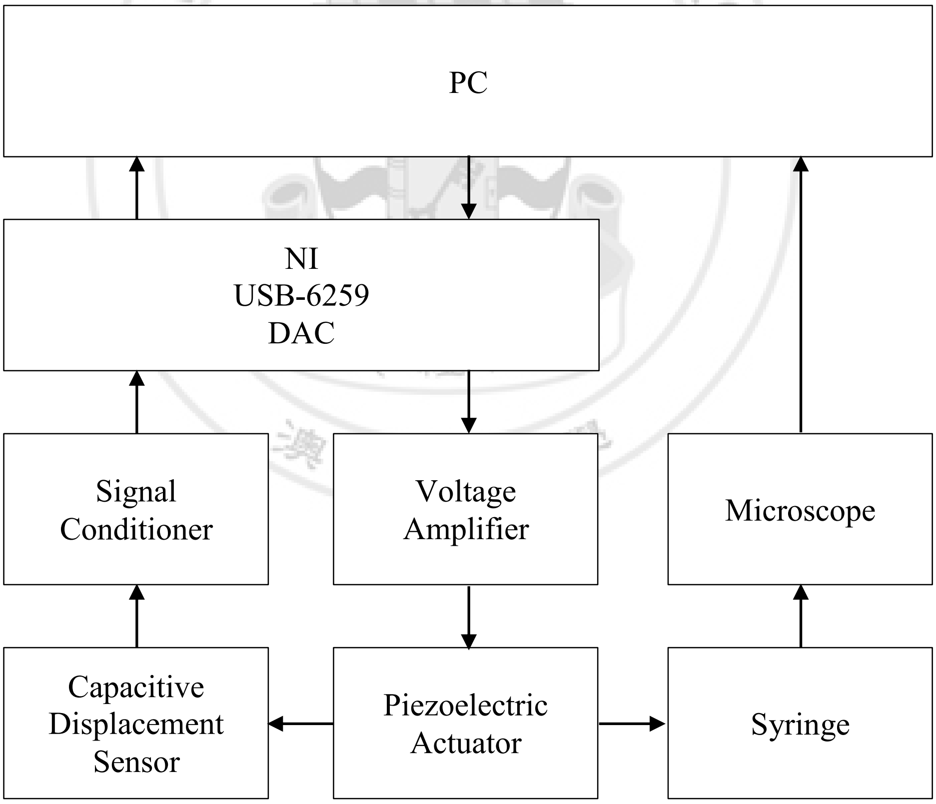

Figure 16: The block diagram of experimental setup

CHAPTER 5: EXPERIMENTS AND DATA PROCESSING

5.1. LABVIEW PROGRAM DEVELOPMENT

LabVIEW is a graphical programming software that can easily build an engineering system, which includes data acquisition, data processing and virtual control panel.

In this project, LabVIEW is used as a virtual PID controller and data collector for sensor and PEA, Figure 17 shows used-components of the program and its wirings, which mainly includes a controller section, a sensor zeroing section and data visualization sections.

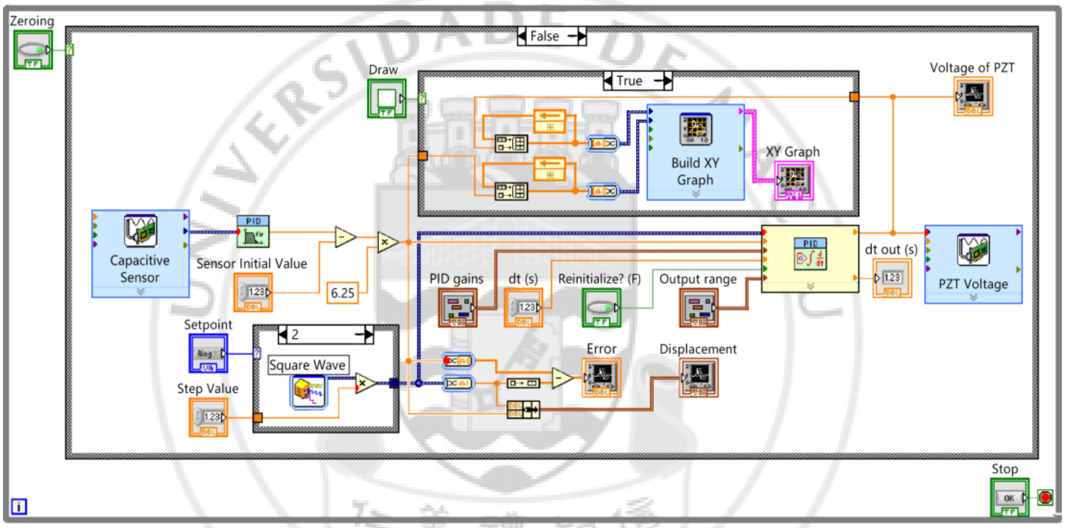

Figure 17: The block diagram (some of the cases are not be shown)

For the convenience of changing those parameters and observing the real time results, each of the function panels has been arranged to one screen. Figure 18 shows the arrangement of each function panel.

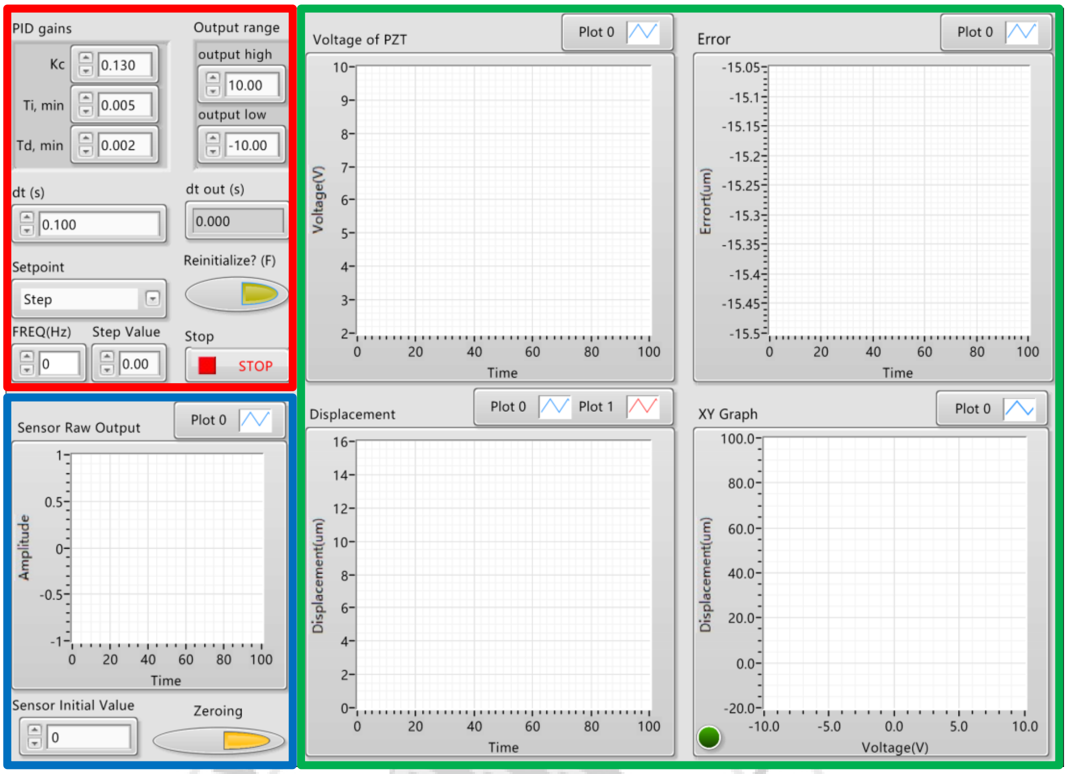

Kc 0.130
Ti, min 0.005
Td, min 0.002
output high 10.00
output low -10.00
dt (s) 0.100
dt out (s) 0.000
Setpoint Step
FREQ(Hz) 0
Step Value 0.00
Sensor Initial Value 0

Figure 18: The control panel of the LabVIEW program includes sensor zeroing panel (in blue), parameter setting panel (in red) and graph panel (in green), and those parameters' value are not the final set.

5.2. GAINS TUNING FOR CONTROLLER

Tuning the gains of a PID controller is the most challenge part of this experiment, there are some proven methods such as Ziegler–Nichols method [27], Tyreus Luyben method [28] and Cohen-Coon method [29]. However, there is not a method can deal with every system since different systems have its own characteristics. In order to have a balanced performance, manual tuning is a conservative choice but it is also effective and easy to process.

After testing and comparing, the gains were finally tuned to passable values as shown in Table 5, the following experiments is based on these gains:

Table 5: The gains of PID controller

K_c	0.140
$T_i(min)$	0.004
$T_d(min)$	0.001
$dt(s)$	0.100

5.3. EQUIPMENT PERFORMANCE

5.3.1. OPEN-LOOP TEST

Before the close-loop test, the open-loop test is necessary to be done to verify the relationship between input and output. Figure 19 shows the step response when the system is applied a 1-V input (the value will be 10-time-amplified, and then acting on the PEA, the same below):

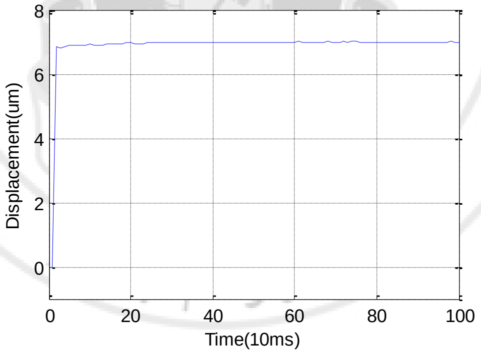

Figure 19: The output under a 1-V input

5.3.2. CLOSE-LOOP TEST

In the close-loop test, the first experiment is to test the maximum output of the main structure, a 0.1-Hz sinusoidal signal with 5-V amplitude and 5-V offset is applied to the PEA, the result can be determined as shown in Figure 20:

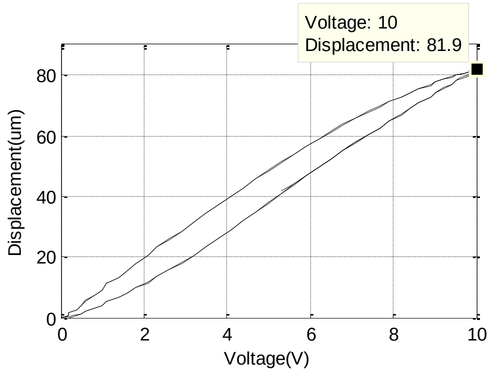

Figure 20: The relationship between the displacement and the voltage

The actual output is 81.9-µm which is 80.15% of the simulation result (102.18-µm), the possible reasons of the gap between the actual and simulation result will be discussed in Chapter 6.

The second experiment is to observe the dynamic characteristic of this system, including a step response test and two sinusoidal motion tracking tests in different frequencies. In the step response test, there is a step signal from 0 to 50-µm, Figure 21 shows the actual output, voltage change and error during the test:

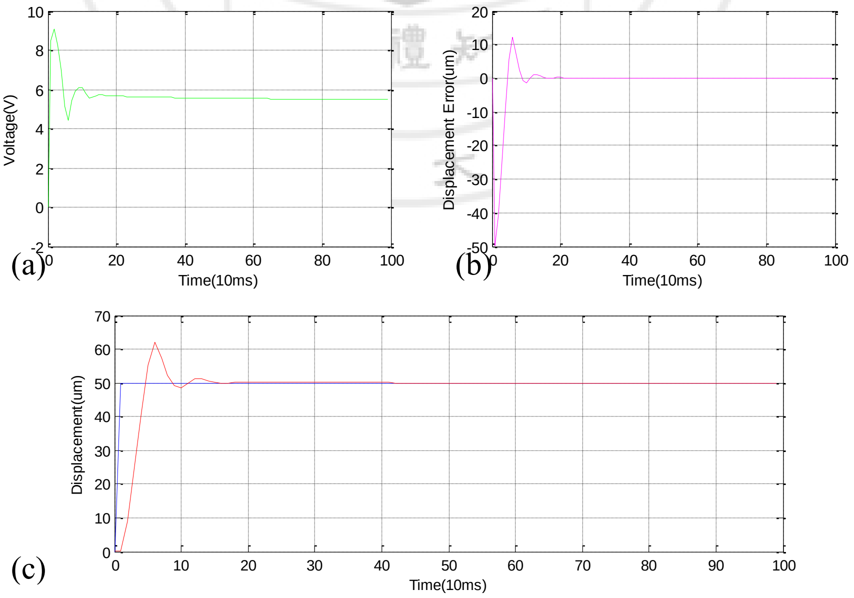

Figure 21: (a) The voltage change (in green) during the process; (b) The error (in magenta) during the process; (c) The output (in red) and setpoint (in blue)

The next step is giving sinusoidal signals to the controller, there are two signals that one's frequency is 0.5-Hz and another one is 5-Hz with the same 40-μm amplitude and 40-μm offset.

By comparing Figure 22 and 23, obviously, the system works well in low frequency, but the high frequency performance is no good. With a higher frequency, the delay is more obvious, which is also causing larger error and more serious hysteresis effect. It may be the gains' problem in the controller since the performance can be better if the gains are specially re-tuned for high frequency, but the performance may be worse in other situations.

To solve the problem, it needs advance control algorithms, which is an improving direction in the future research.

The third test is to verify the system resolution, which is important for determining the minimum range that the system can react. The process is to decrease the amplitude of the square wave, until found the least amplitude which can still distinguish the peaks and valleys. Figure 24 indicates the resolution is around 5-nm.

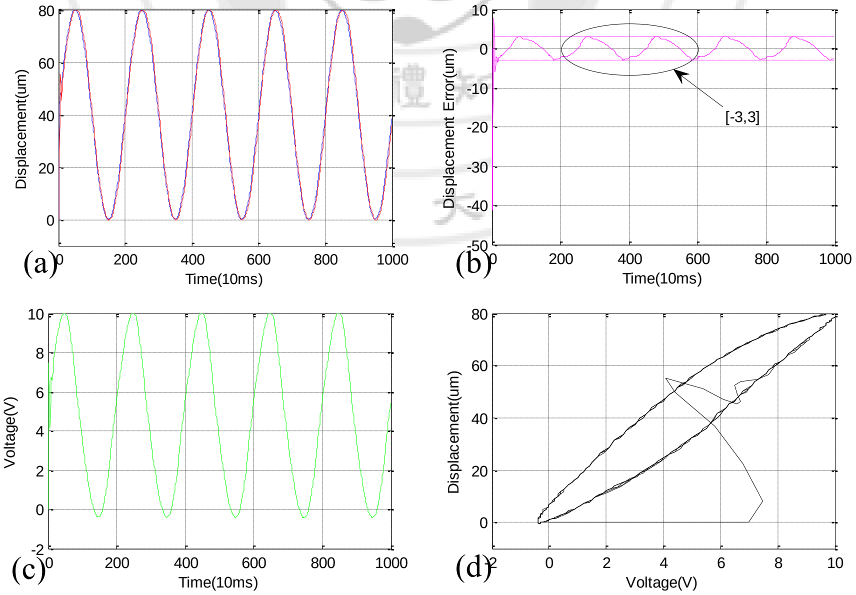

Figure 22: Under a 0.5-Hz sinusoidal signal: (a) The output (in red) and setpoint (in blue); (b) The error (in magenta) during the process; (c) The voltage change (in green) during the process; (d) The hysteresis loop (in black)

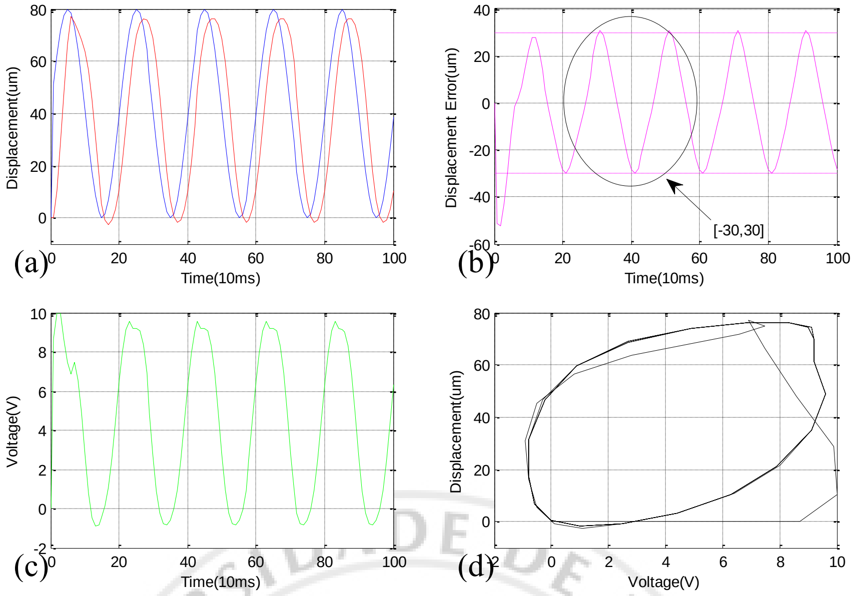

Figure 23: Under a 5-Hz sinusoidal signal: (a) The output (in red) and setpoint (in blue); (b) The error (in magenta) during the process; (c) The voltage change (in green) during the process; (d) The hysteresis loop (in black)

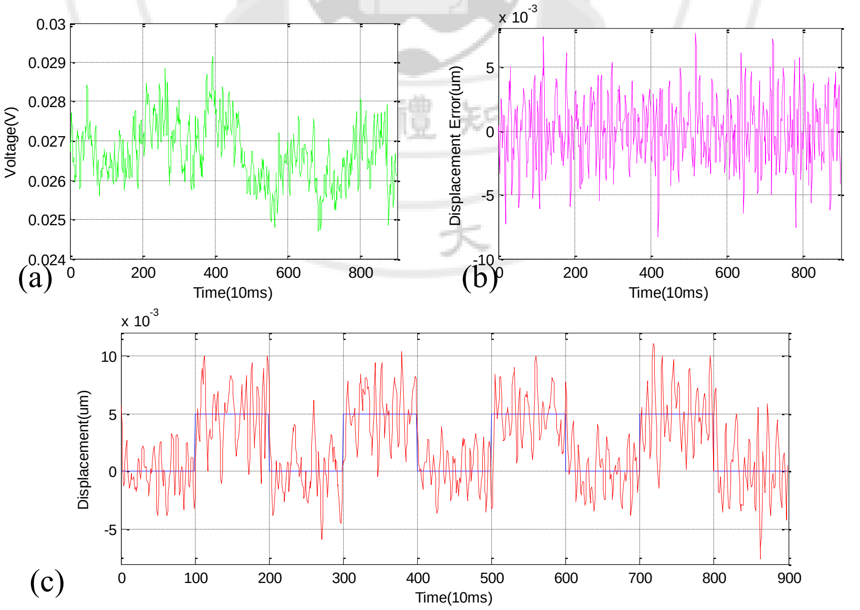

Figure 24: (a) The voltage change (in green) during the process; (b) The error (in magenta) during the process; (c) The output (in red) and setpoint (in blue)

5.4. SYRINGE OUTPUT DATA PROCESSING

Those results in Chapter 5.3 and 5.4 are all based on the data from the capacitive sensor, which means it is only representing the performance of the main structure. To verify the actual performance of the micro-syringe pump, a microscope is used in order to observe the output in the tube and capture the pictures.

Figure 25: The microscope and the tube

5.4.1. LIQUID LEVEL IDENTIFICATION

Because of the capillarity in a small tube, the actual liquid surface position cannot be measured directly, therefore, it needs a method to calculate the surface position.

Assume the liquid surface is spherical, some necessary parameters can be measured directly from the picture as shown in Figure 26. They are the diameter of the tube D, the radius of liquid surface r, the contact angle θ and the height of spherical surface h. Applying the sine law:

$$\frac{D}{sin\theta} = \frac{r}{sin(90° - \theta)}, \tag{13}$$

thus:

$$r = \frac{Dcos\theta}{sin2\theta}. \tag{14}$$

Put the yellow dash line as y-axis, the black dash line as x-axis and its center as origin, build a rectangular coordinate system, then the curve of liquid surface in center section can be express as:

$$x^2+\left[y+\left(\frac{Dcos\theta}{sin2\theta}-h\right)\right]^2=\left(\frac{Dcos\theta}{sin2\theta}\right)^2, \tag{15}$$

after that, the volume of spherical part can be calculated as:

$$V=\int_0^h \pi\left\{\left(\frac{Dcos\theta}{sin2\theta}\right)^2-\left[y+\left(\frac{Dcos\theta}{sin2\theta}-h\right)\right]^2\right\}dy, \tag{16}$$

then the actual height is:

$$H=\frac{V}{\pi({}^{D}/_{2})^2}, \tag{17}$$

combining Eq. (16) and Eq. (17), the actual height of a convex surface is:

$$H=\frac{4}{D^2}\int_0^h\{(h-y)(Dcsc\theta-h+y)\}\ dy, \tag{18}$$

and if it is a concave surface, Eq. (18) can be modified as:

$$H=h-\frac{4}{D^2}\int_0^h\{(h-y)(Dcsc\theta-h+y)\}\ dy. \tag{19}$$

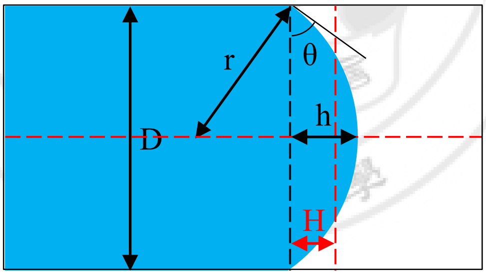

Figure 26: The parameters when the liquid in a small tube

5.4.2. SYRINGE OUTPUT

For measuring the output in the tube, there are only a microscope can be used, it limits what can be done with the output. However, a range test still can be processed. In the test, a 0.1-Hz sinusoidal signal with 5-V amplitude and 5-V offset is applied to the PEA.

Given that the inner radius of the tube is 0.8-mm, which be as the measuring scale. Figure 27 shows the processed pictures and its analyses based on Eq. (18) and (19). The vertical red lines in Figure 27(d) are the actual liquid level of the “valley” and “peak”, and the distance between these two lines is measured as the output range, which is 8.64-mm. The data are measured by analyzing Figure 27(a) and (b), which are resulting in Table 6.

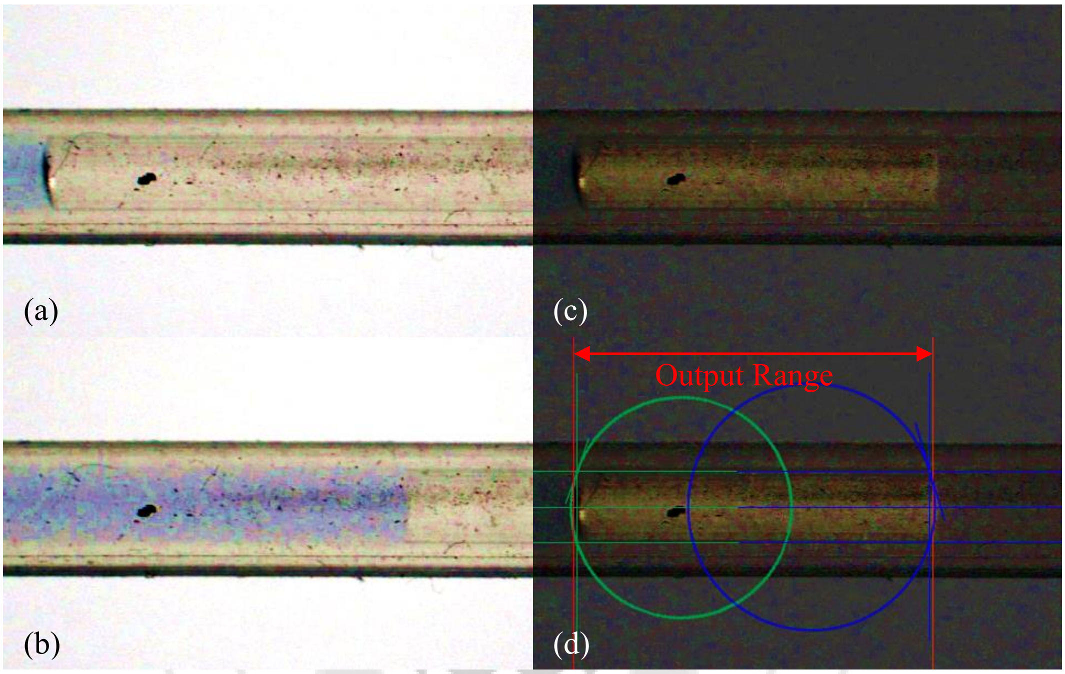

Figure 27: The processed picture. (a) The "valley"; (b) The "peak"; (c) The merged picture (d) The analysis to the merged picture

Table 6: The data by pictures analyzing

	“Valley”	“Peak”
$\theta(degree)$	19.5	16.7
$D(mm)$	0.8	0.8
$h(mm)$	0.074419	0.060465
$H(mm)$	0.0338	0.031349
$Output\ Range(mm)$	8.64	

The inner radius of syringe is measured and its value is 12.5-mm, therefore, it should have about 244.14 times’ amplification factor between the main structure and the tube by a simple calculation, which means there should be a 244.14×81.9-um≈20.00-mm output in the tube.

But referring to the actual output of the main structure and the tube, the actual amplification factor is only about 105.49 times, which is much less than the calculated factor. The difference should be attributable to the syringe, and it will be discussed in Chapter 6.

It is necessary to know the minimum volume of liquid that the micro-syringe pump can deliver, but due to the lack of the relay equipment, it can only be estimated. Assume the syringe is a linear system, the minimum volume can be expressed as:

$$V_{minimum} = Resolution * \begin{array}{c} Amplification \\ fator \end{array} * \begin{array}{c} Tube \\ sectional. \\ area \end{array} \qquad (20)$$

Therefore, based on a 5-nm resolution of the main structure and 105.49 times’ amplification factor of the syringe, the minimum volume is about 0.265-nL, and the maximum volume is also calculated as a result of 4.34-μL. Since the micro-syringe pump still can be further improved, it should have a big potential to work better.

CHAPTER 6: DISCUSSION

In comparison with FEA simulation result, the experimental result of motion output is smaller. Because the manufacturing tolerances are difficult to avoid, especially for a multiple parameters system, the slight differences of each parameter may significantly influence its performance. Moreover, the fabrication method also affects the results. For example, in the FEA simulation, the amplifier and CPF are integrated as one part, but in practice, the amplifier is connected to CPF by screws, and a thin sheet of metal is placed as the interface of PEA and crews.

The zeroing of the capacitive sensor is an important pre-operate step which is to manually record the sensor's output value in rest, then apply the value as the initial value. However, due to the existence of zero drift, it is difficult to obtain the value exactly. Therefore, the output precision depends on the precision of the sensor zeroing.

It is believed that the syringe is the biggest factor affecting the results. The syringe is pushed by the plunger while changing liquid flow, increasing pressure in the fluidic system could oppose the liquid into motion and increase the input stiffness of the main structure. Then it affects the frequency and the stock of PEA according to Eq. (21) and (22):

$$f = \sqrt{k/m}, \tag{21}$$

$$x' = \frac{x k_{PZT}}{k_{PZT} + k_{Sturcture}}. \tag{22}$$

Because of the deformation of the rubber part of the syringe, the output in tube is much smaller than the computational results. It compresses the rubber, then pushes the liquid, which is observed in the output range testing experiment.

Environmental conditions also influence the performance of most force-control mechanical pumps, such as temperature and fluid viscosity. They impact the accuracy of the syringe pump.

Since there is not an effective method to measure the liquid surface position, the results may have a huge error due to the operator of data processing. To reduce the measurement error, there should be a new method and device to do the job.

The performance of the micro-syringe pump depends on the control method and parameters. The control method used in this project is PID control. In order to obtain a better result, a set of more suitable gains of PID controller needs to be achieved. Nevertheless, in view of the hysteresis of PEA, the performance of PID control is not stable enough at high frequency operation.

Overall, unlike other bulky and easily disturbed drivers, the micro-syringe pump designed in this project has demonstrated large benefits, such as compact, simple, and easy-to-use, and it can obtain various flow rates accurately and consistently by using common syringes. Furthermore, in view of the performance, it is able to achieve the steady state within a much less time. The stable and accurate displacement output can be achieved with a 5-nm resolution of the system. It is easier to get reproducible and exploitable scientific results when using the micro-syringe pump.

CHAPTER 7: CONCLUSION

This thesis presents the design, optimization and control of a micro-syringe pump, which is mostly focused on the design and optimization of the main structure. A parameterized CAD model is optimized by applying adaptive single-objective method to obtain the highest frequency. To verify the optimal results, a simulation is used to examine the performance.

A LabVIEW program is developed to do the control and data processing experiments. For the experiments, a prototype is fabricated. The experimental results demonstrate the performance of the micro-syringe pump. An expression of the actual liquid height is derived to help in measuring the output of the micro-syringe pump. An error analysis is carried out to discuss the difference between simulation and actual results.

In the future work, an advanced control algorithm will be implemented to control the micro-syringe pump for use in different situations.

REFERENCES

[1] W. Zeng, S. Li, and Z. Wang, "Characterization of syringe-pump-driven versus pressure-driven microfluidic flows," in *Fluid Power and Mechatronics (FPM), 2015 International Conference on*, 2015, pp. 711-715.

[2] A.-W. A. Saif, A. S. Shbair, and W. K. Zaitouni, "Auto-Syringe system for chemical applications using micro-controller," in *Computer Applications and Industrial Electronics (ICCAIE), 2010 International Conference on*, 2010, pp. 104-109.

[3] M. M. Teymoori and E. Abbaspour-Sani, "Design and simulation of a novel electrostatic peristaltic micromachined pump for drug delivery applications," *Sensors and Actuators A: Physical*, vol. 117, pp. 222-229, 2005.

[4] A. Ichikawa, T. Tanikawa, K. Matsukawa, S. Takahashi, and K. Ohba, "Fluorescent monitoring using microfluidics chip and development of syringe pump for automation of enucleation to automate cloning," in *Robotics and Automation, 2009. ICRA'09. IEEE International Conference on*, 2009, pp. 2231-2236.

[5] G. Liu, Z. Yang, J. Liu, X. Li, H. Wang, T. Zhao, *et al.*, "A low cost, high performance insulin delivery system based on PZT actuation," *Microsystem Technologies*, vol. 20, pp. 2287-2294, 2014.

[6] A. Nisar, N. Afzulpurkar, B. Mahaisavariya, and A. Tuantranont, "MEMS-based micropumps in drug delivery and biomedical applications," *Sensors and Actuators B: Chemical*, vol. 130, pp. 917-942, 2008.

[7] W. Zhao, Q. Wang, Q. Zhan, J. Zhuang, X. Ning, and J. Yin, "Design of a portable insulin syringe based on MSP430 MCU," in *Biomedical Engineering and Informatics (BMEI), 2010 3rd International Conference on*, 2010, pp. 1459-1462.

[8] (April 18th). *Syringe pumps and microfluidics 2014 - Elveflow*. Available: http://www.elveflow.com/microfluidic-tutorials/microfluidic-reviews-and-tutorials/syringe-pumps-and-microfluidics/

[9] K. Akash, M. P. Kumar, N. Venkatesan, and M. Venkatesan, "A single acting syringe pump based on Raspberry Pi??? SOC," in *2015 IEEE International Conference on Computational Intelligence and Computing Research (ICCIC)*, 2015, pp. 1-3.

[10] Y. Tanaka, K. Doumoto, A. Sano, and H. Fujimoto, "Development of a sensor system with syringe based on tactile sensing using balloon expansion," in *Robotics and Automation (ICRA), 2010 IEEE International Conference on*, 2010, pp. 4861-4866.

[11] R. Assuncao, P. Barbosa, R. Ruge, P. Guimaraes, J. Alves, I. Silva, *et al.*, "Developing the control system of a syringe infusion pump," in *Remote Engineering and Virtual Instrumentation (REV), 2014 11th International Conference on*, 2014, pp. 254-255.

[12] D. A. Henderson, "Novel piezo motor enables positive displacement microfluidic pump," *Stroke (mm)*, vol. 50, p. 10, 2007.

[13] K. Kuroda, S. Sakuma, F. Arai, and M. Kaneko, "High-speed cell manipulation by backlashless syringe pump," in *Ubiquitous Robots and Ambient Intelligence (URAI), 2013 10th International Conference on*, 2013, pp. 148-150.

[14] T. M. Rideout, J. R. LaCourse, and P. L. McWilliam, "Force sensing syringe as a teaching tool for injection," in *Bioengineering Conference (NEBEC), 2012 38th Annual Northeast*, 2012, pp. 364-365.

[15] T. Dolzan, D. Vrtacnik, D. Resnik, U. Aljancic, M. Mozek, B. Pecar, *et al.*, "Design of transdermal drug delivery system with PZT actuated micropump," in *Information and Communication Technology, Electronics and Microelectronics (MIPRO), 2014 37th International Convention on*, 2014, pp. 96-99.

[16] B. Jaffe, *Piezoelectric ceramics* vol. 3: Elsevier, 2012.

[17] (March 09). *Piezo Systems: Piezoceramic, PZT, Piezoelectric Transducers, Piezoelectric Actuators and Sensors, Piezoelectric Fans, Piezoelectric Amplifiers, Piezoelectric Engineering, Ultrasonic Transducers, and Energy Harvesters.* Available: http://www.piezo.com/

[18] K. Junwu, Y. Zhigang, P. Taijiang, C. Guangming, and W. Boda, "Design and test of a high-performance piezoelectric micropump for drug delivery," *Sensors and Actuators A: Physical*, vol. 121, pp. 156-161, 2005.

[19] W. Xu and T. King, "Flexure hinges for piezoactuator displacement amplifiers: flexibility, accuracy, and stress considerations," *Precision engineering*, vol. 19, pp. 4-10, 1996.

[20] Q. Xu and Y. Li, "Analytical modeling, optimization and testing of a compound bridge-type compliant displacement amplifier," *Mechanism and Machine Theory*, vol. 46, pp. 183-200, 2011.

[21] Q. Xu, "New flexure parallel-kinematic micropositioning system with large workspace," *Robotics, IEEE Transactions on*, vol. 28, pp. 478-491, 2012.

[22] X. Tang and I. Chen, "A large-displacement and decoupled XYZ flexure parallel mechanism for micromanipulation," in *Automation Science and Engineering, 2006. CASE'06. IEEE International Conference on*, 2006, pp. 75-80.

[23] S. Awtar and G. Parmar, "Design of a large range XY nanopositioning system," *Journal of Mechanisms and Robotics*, vol. 5, p. 021008, 2013.

[24] S. Lin, Y. Jia, I. P. Lei, and Q. Xu, "Design and optimization of a long-stroke compliant micropositioning stage driven by voice coil motor," in *Control Automation Robotics & Vision (ICARCV), 2012 12th International Conference on*, 2012, pp. 1716-1721.

[25] Y. Liu, K. Wu, D. Xu, and Q. Xu, "Design of a microscope auto-focusing device based on multi-stage leaf spring," in *Information and Automation (ICIA), 2014 IEEE International Conference on*, 2014, pp. 1-6.

[26] G. Chen, X. Han, G. Liu, C. Jiang, and Z. Zhao, "An efficient multi-objective optimization method for black-box functions using sequential approximate technique," *Applied Soft Computing*, vol. 12, pp. 14-27, 2012.

[27] J. G. Ziegler and N. B. Nichols, "Optimum settings for automatic controllers," *trans. ASME*, vol. 64, 1942.

[28] W. L. Luyben, "Simple method for tuning SISO controllers in multivariable systems," *Industrial & Engineering Chemistry Process Design and Development*, vol. 25, pp. 654-660, 1986.

[29] G. Cohen and G. Coon, "Theoretical consideration of retarded control," *Trans. Asme*, vol. 75, pp. 827-834, 1953.

APPENDIX A: MODEL ANALYSIS RESULTS

In Chapter 3, a FEA is employed to verify the performance. By the model analysis, the first six resonant frequencies of the main structure are listed below:

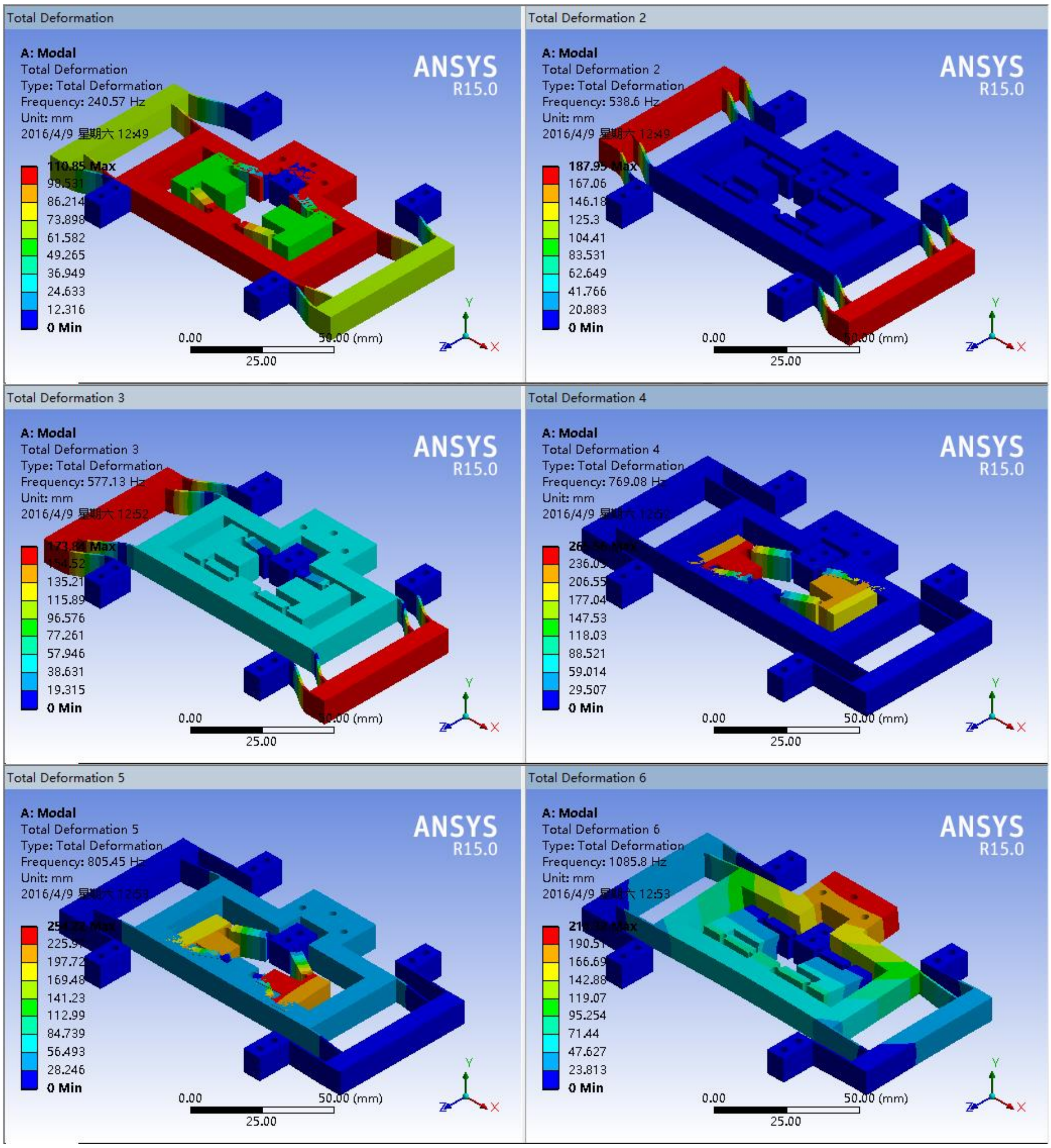
Total Deformation
A: Modal
Total Deformation
Type: Total Deformation
Frequency: 240.57 Hz
Unit: mm
2016/4/9 星期六 12:49

Total Deformation 2
A: Modal
Total Deformation 2
Type: Total Deformation
Frequency: 538.6 Hz
Unit: mm
2016/4/9 星期六 12:49

Total Deformation 3
A: Modal
Total Deformation 3
Type: Total Deformation
Frequency: 577.13 Hz
Unit: mm
2016/4/9 星期六 12:52

Total Deformation 4
A: Modal
Total Deformation 4
Type: Total Deformation
Frequency: 769.08 Hz
Unit: mm

Total Deformation 5
A: Modal
Total Deformation 5
Type: Total Deformation
Frequency: 805.45 Hz
Unit: mm

Total Deformation 6
A: Modal
Total Deformation 6
Type: Total Deformation
Frequency: 1085.8 Hz
Unit: mm
2016/4/9 星期六 12:53

Figure 28: The first six resonant frequencies of the main structure

APPENDIX B: CAD DRAWINGS FOR THE MICRO-SYRINGE PUMP

In this project, the design is drawn by SOLIDWORKS, the drawings of components are listed below.

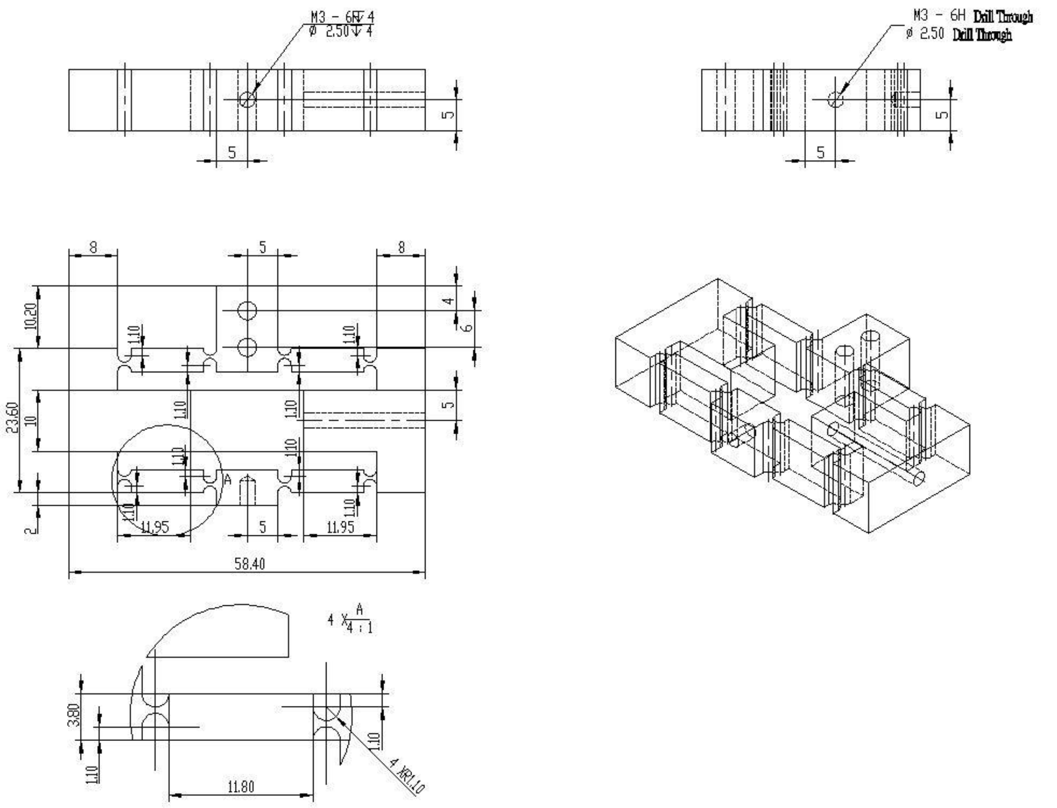

Figure 29: Amplifier

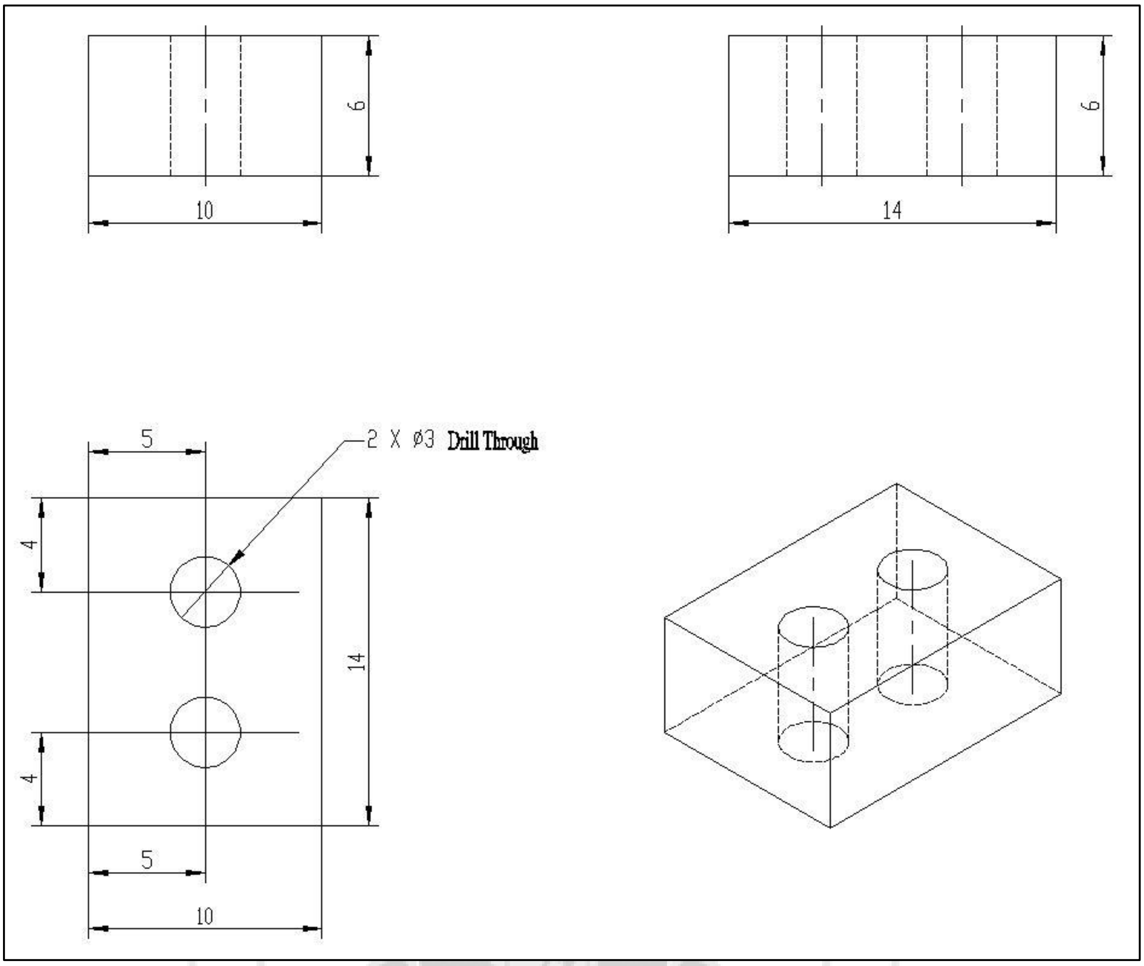

Figure 30: Amplifier Spacer

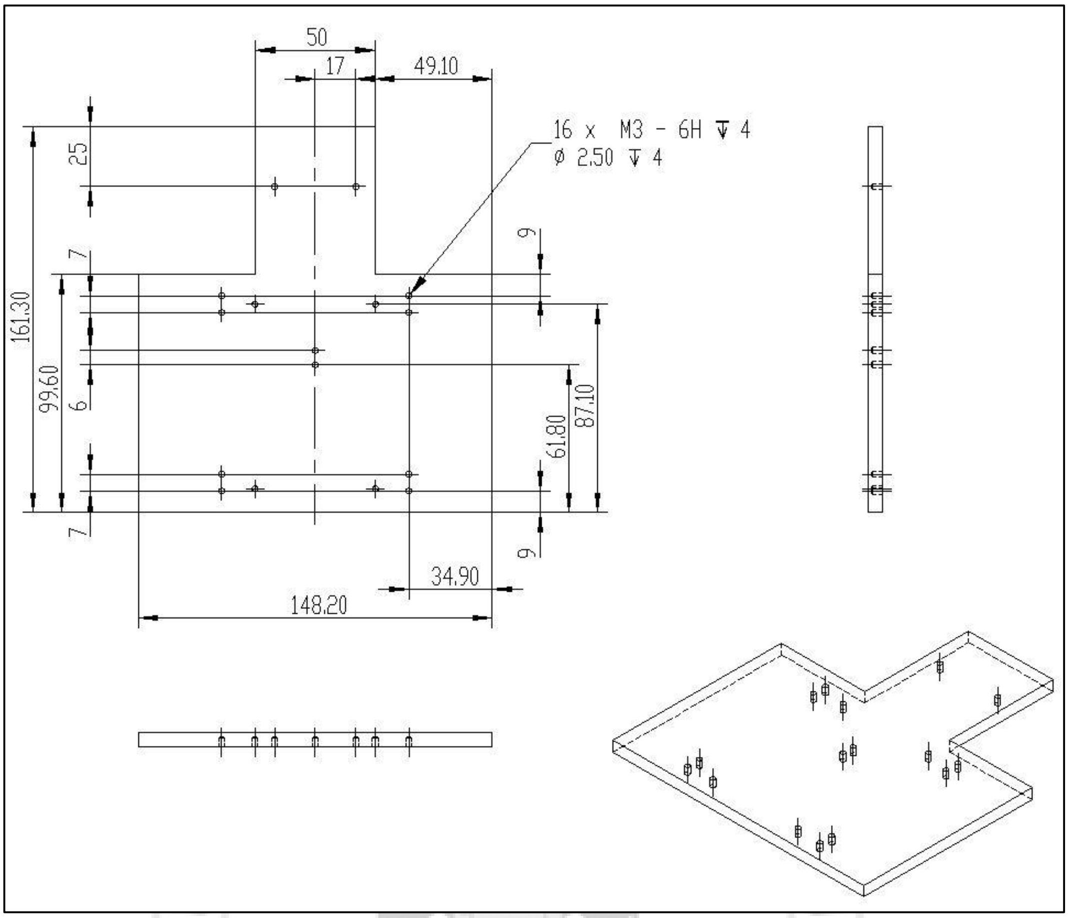

Figure 31: Base

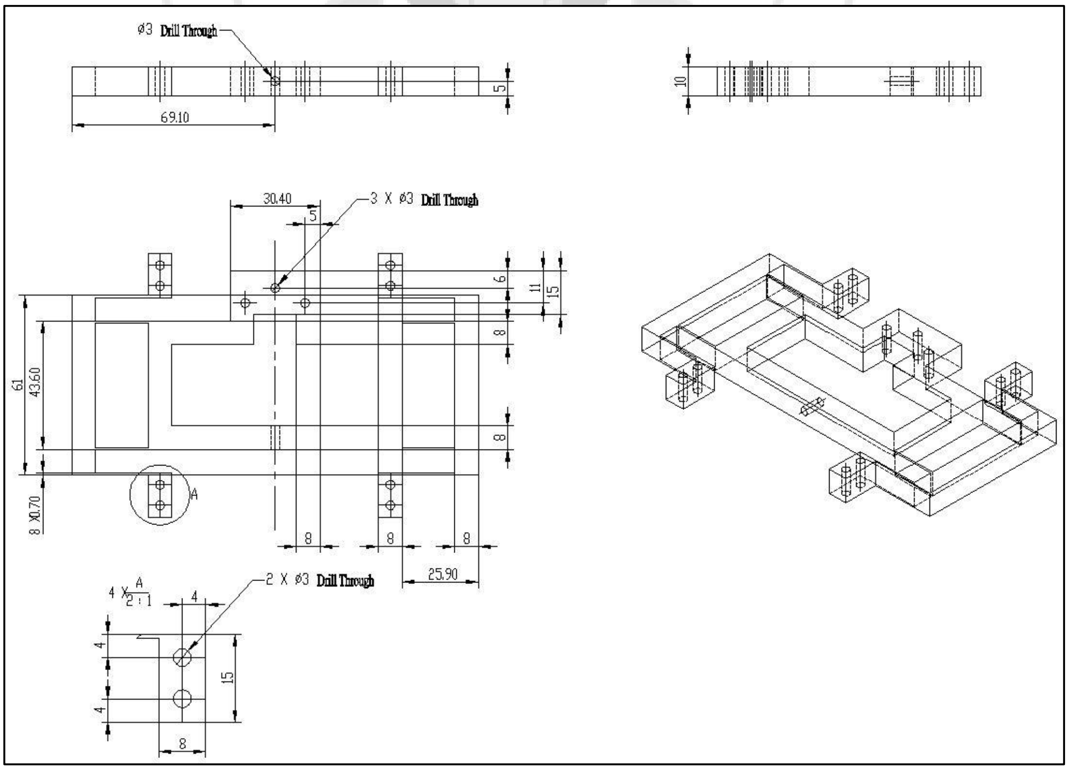

Figure 32: CPF

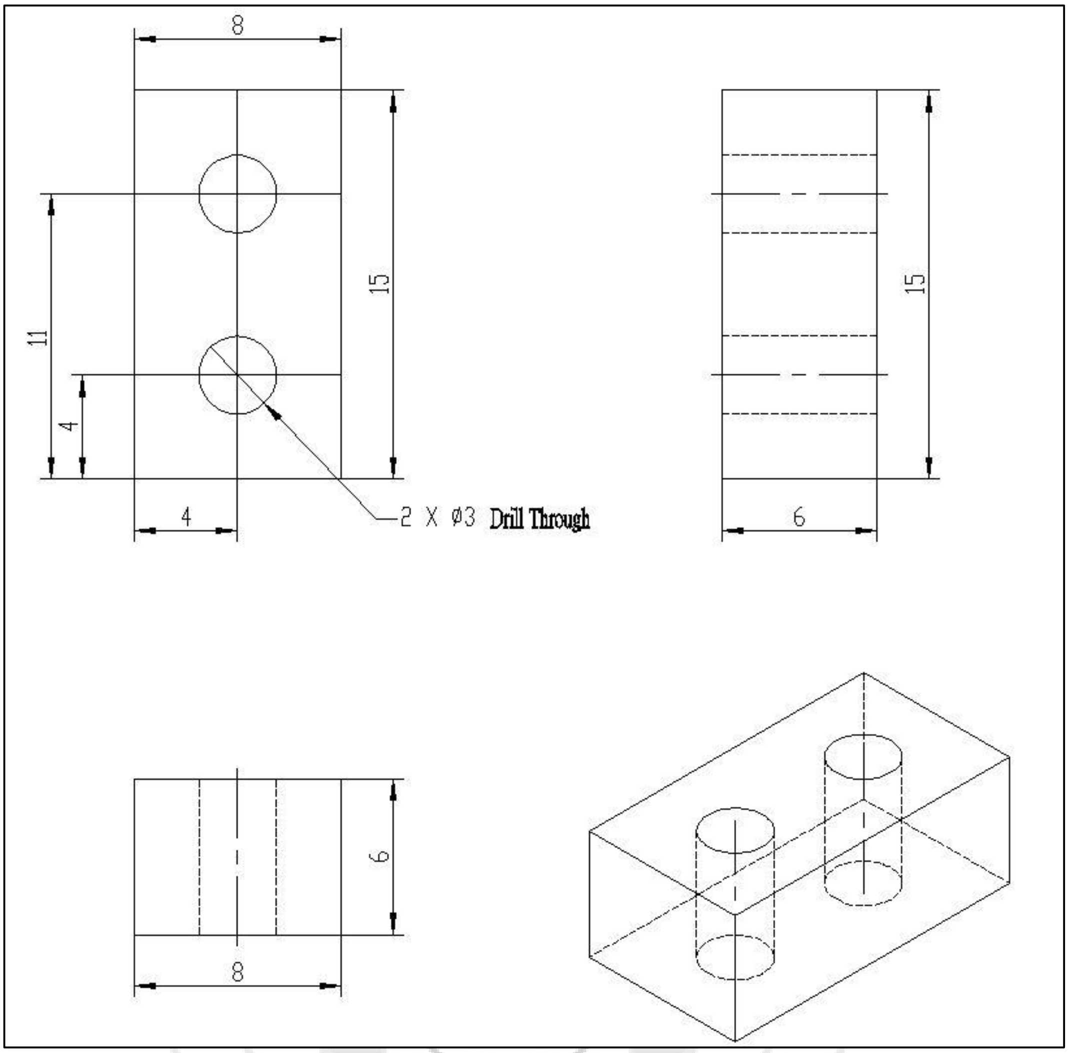

Figure 33: CPF Spacer

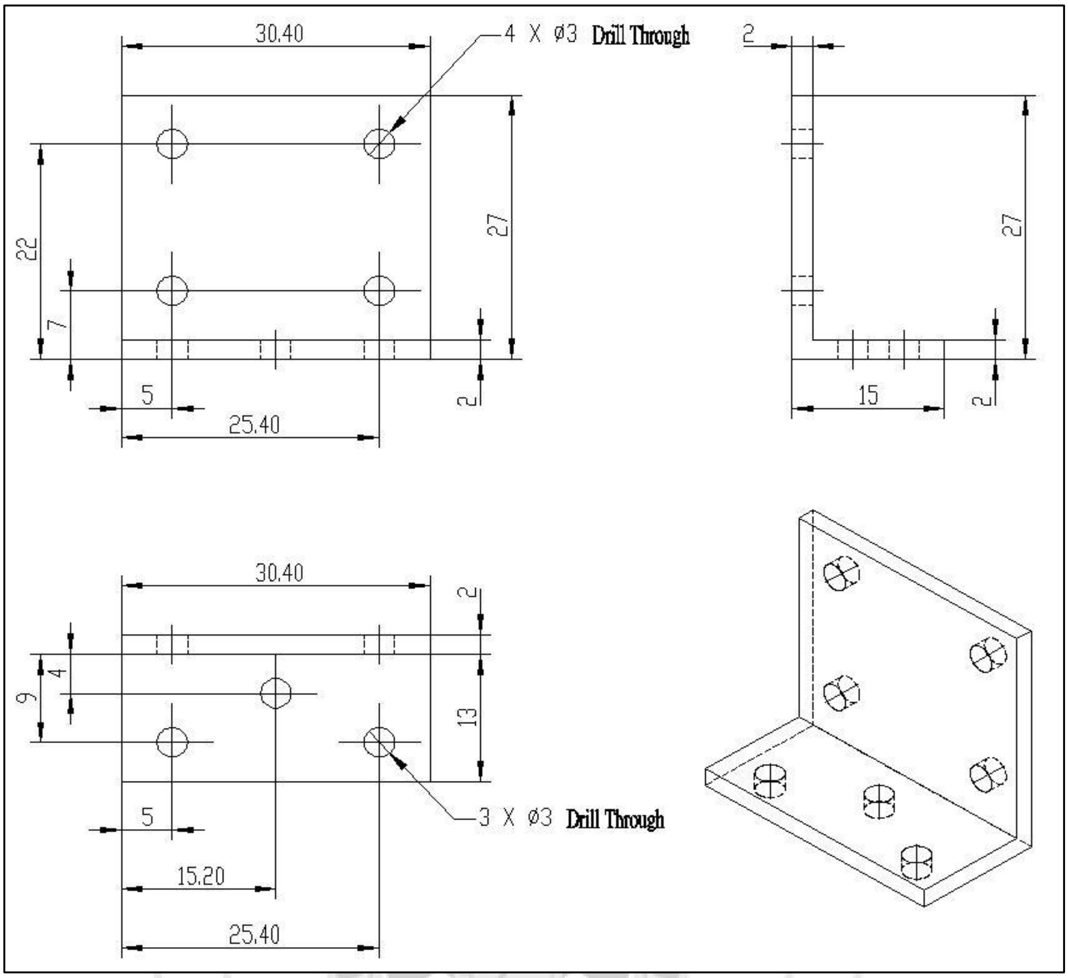

Figure 34: L Shape Connector

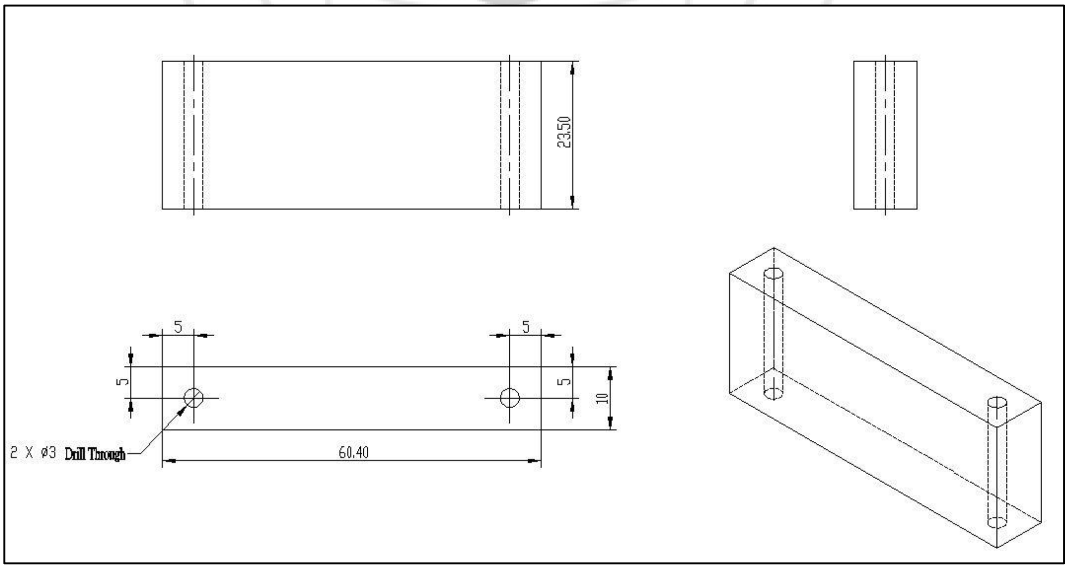

Figure 35: Sensor Support Frame Pillar Long

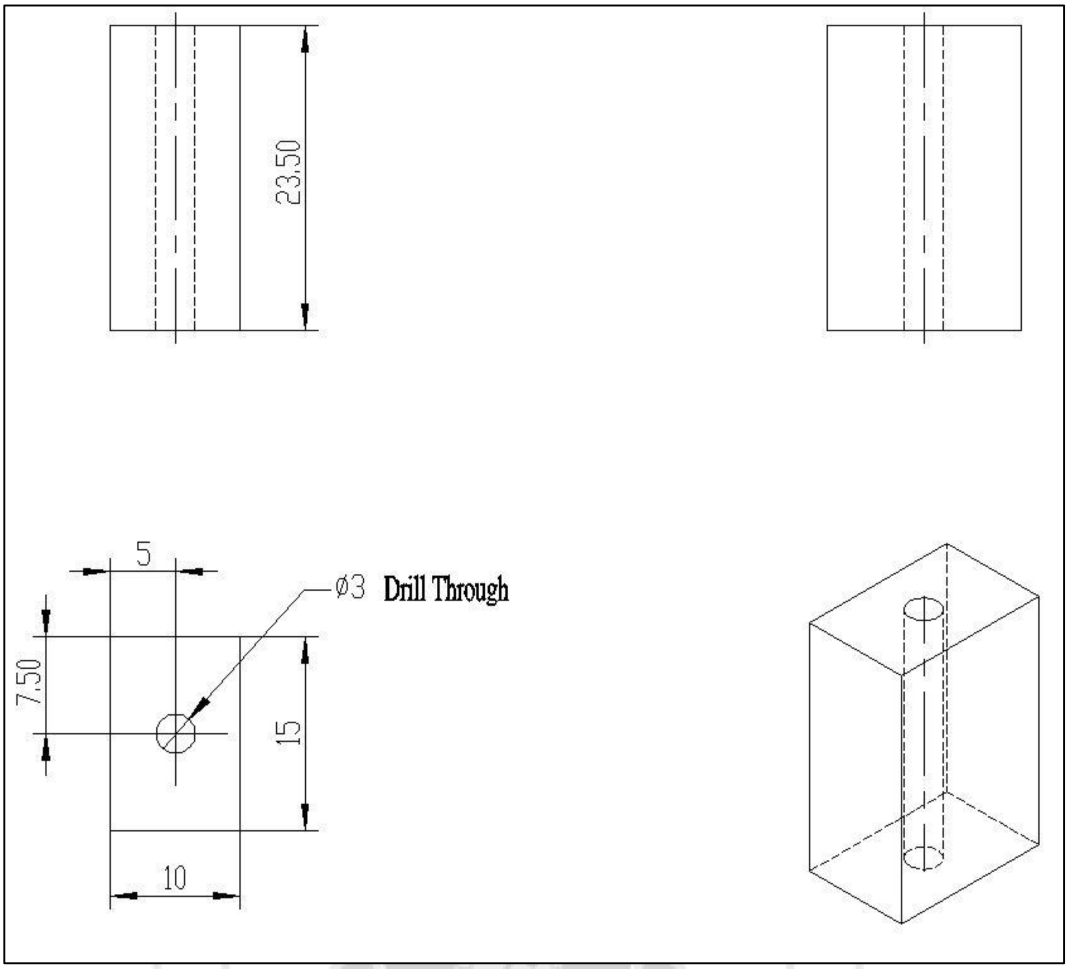

Figure 36: Sensor Support Frame Pillar Short

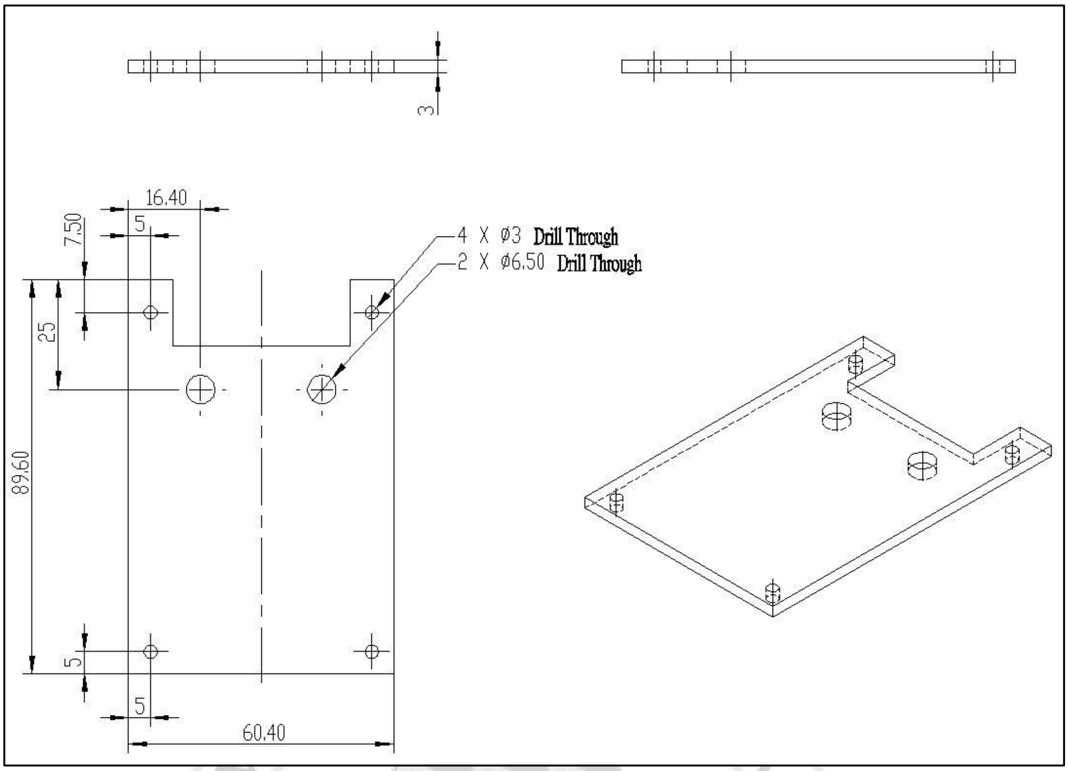

Figure 37: Sensor Support Frame Bracket

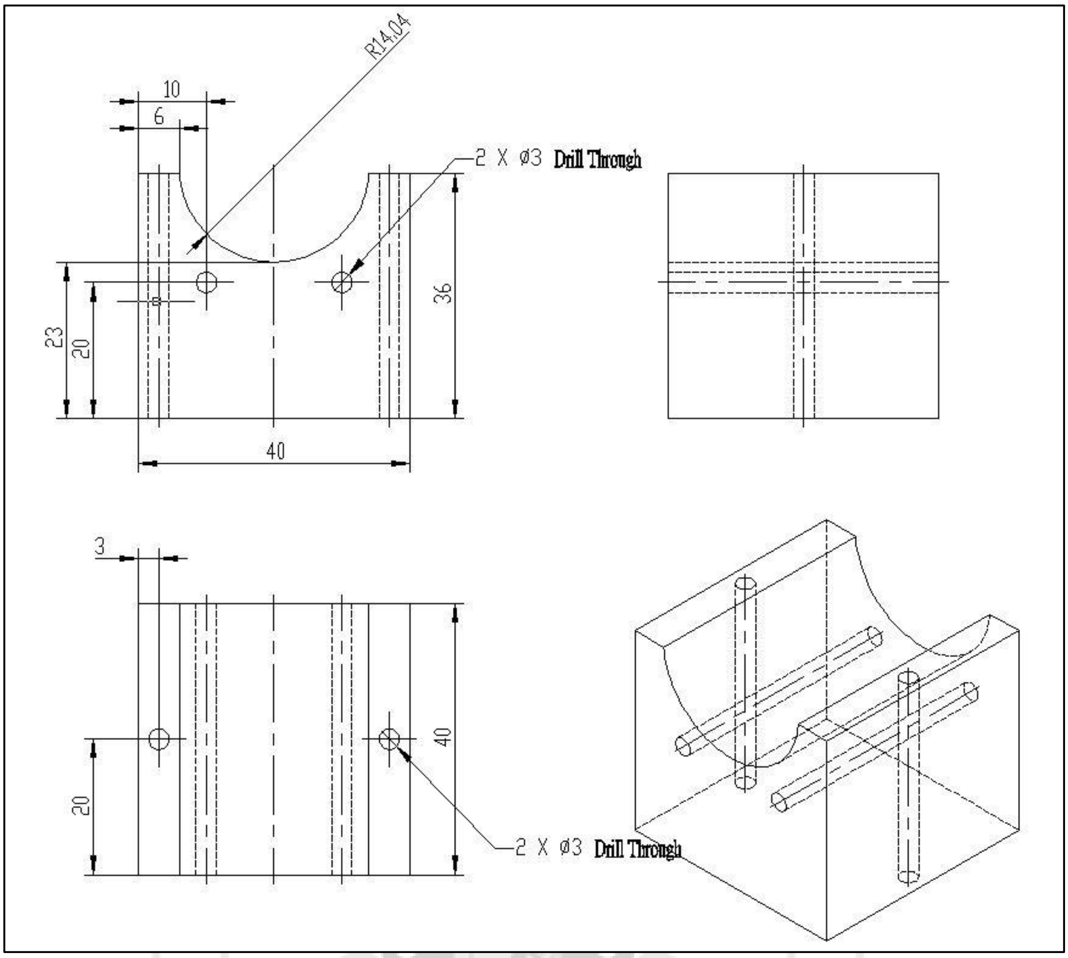

Figure 38: Syringe Bracket

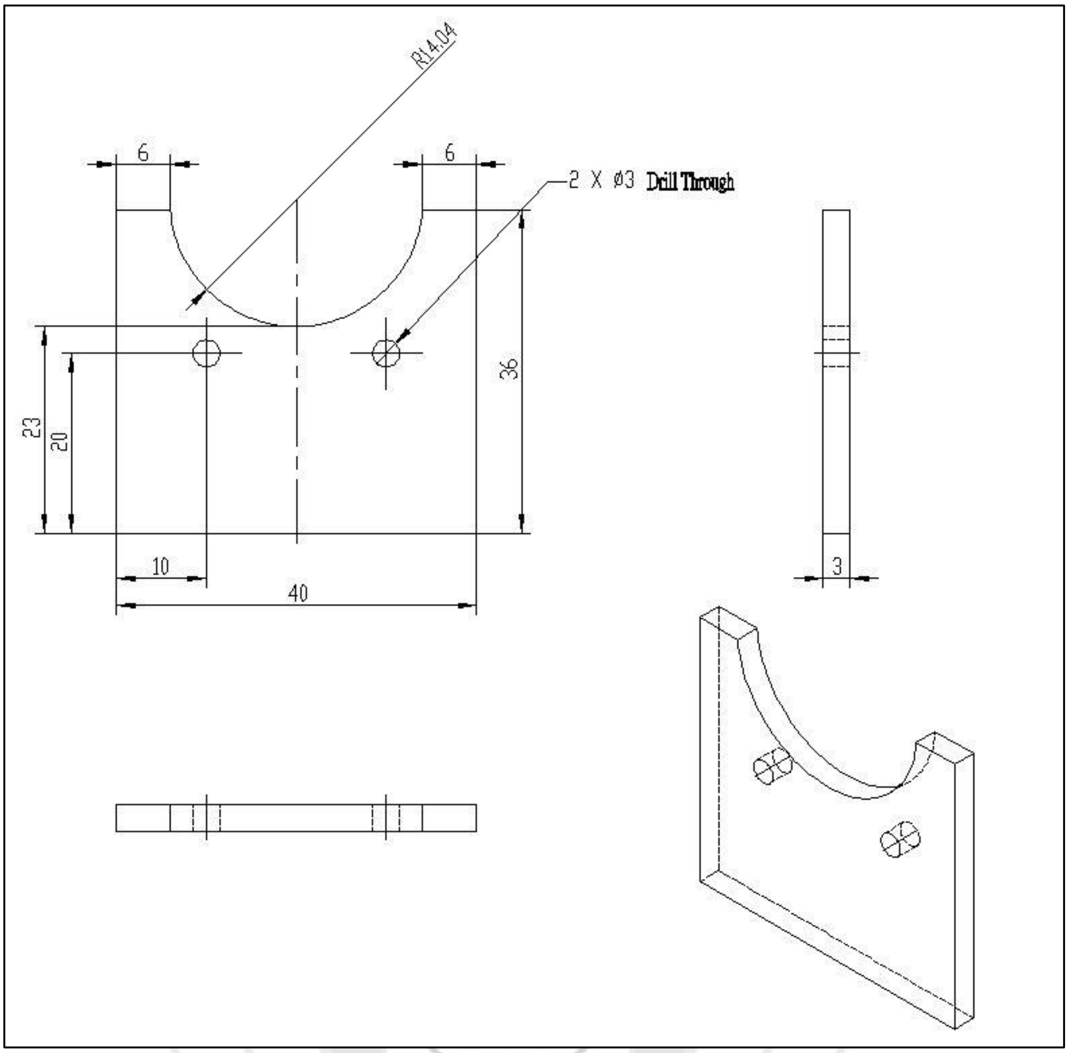

Figure 39: Syringe Outer Barrel Fixture Front

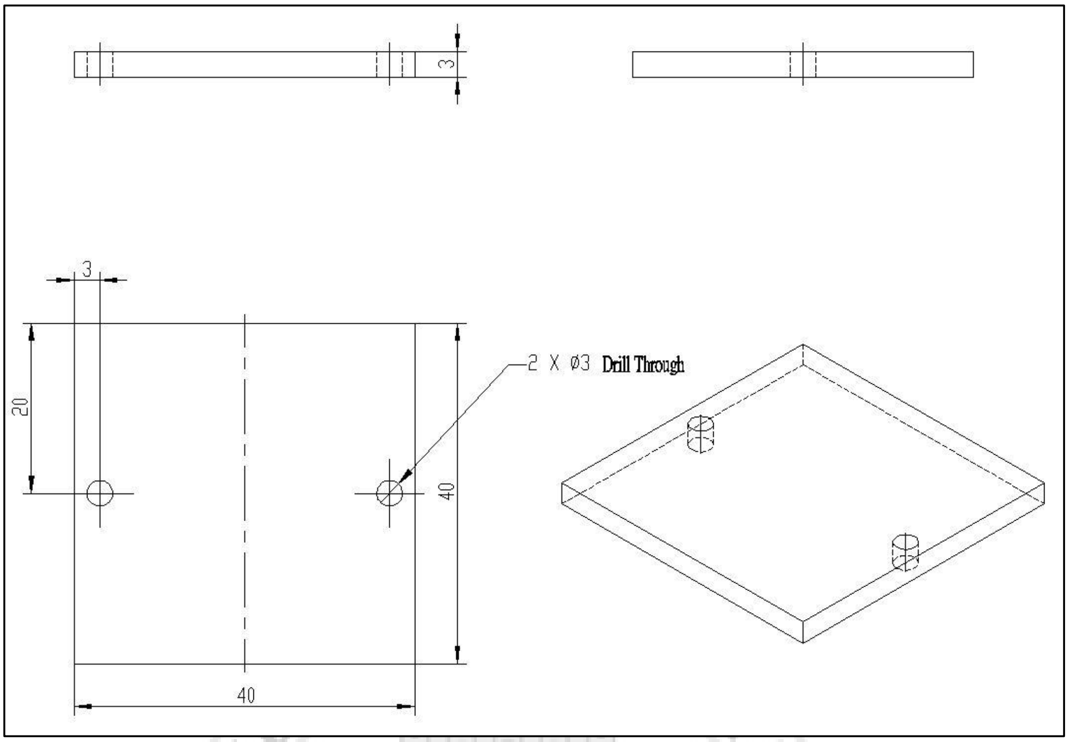

Figure 40: Syringe Outer Barrel Fixture Top

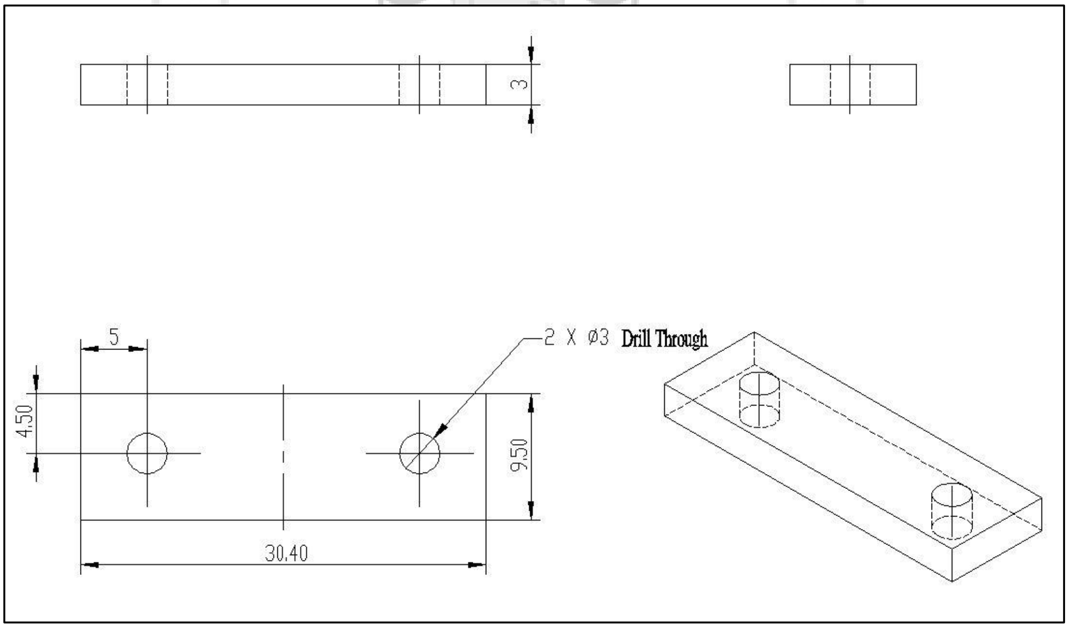

Figure 41: Syringe Push Rob Fixture

APPENDIX C: COMPONENTS LIST OF THE MICRO-SYRINGE PUMP

The components used to fabricate the macro-syringe pump are listed below:

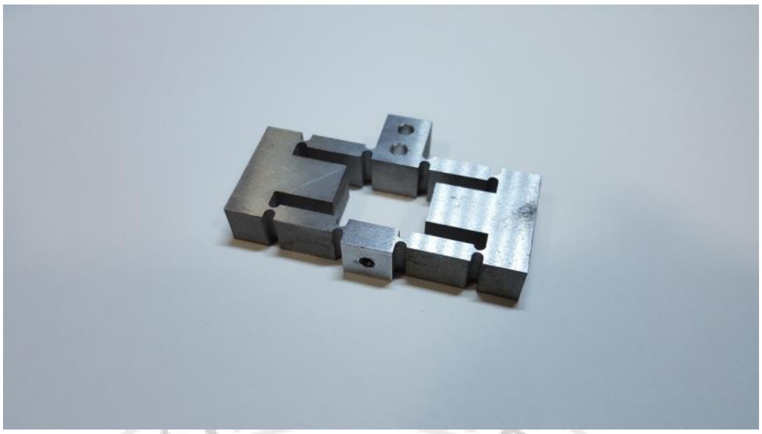

Figure 42: Amplifier

Figure 43: Amplifier Spacer

Figure 44: Base

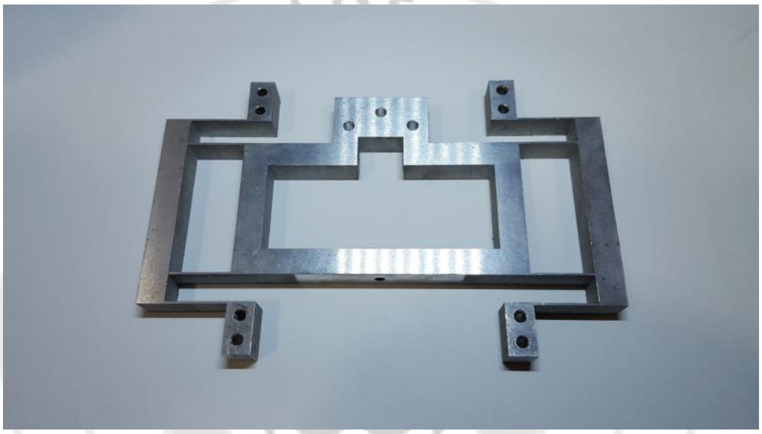

Figure 45: CPF

Figure 46: CPF Spacer

Figure 47: L Shape Connector

Figure 48: Sensor Fixture

Figure 49: Sensor Support Frame Bracket

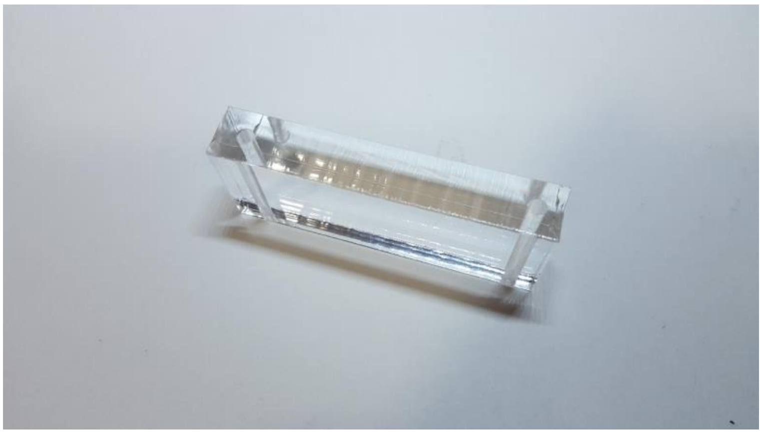

Figure 50: Sensor Support Frame Pillar Long

Figure 51: Sensor Support Frame Pillar Short

Figure 52: Syringe

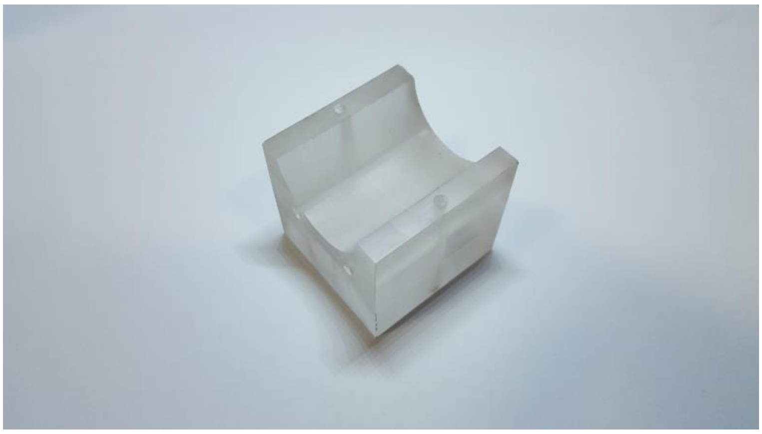

Figure 53: Syringe Bracket

Figure 54: Syringe Outer Barrel Fixture Front

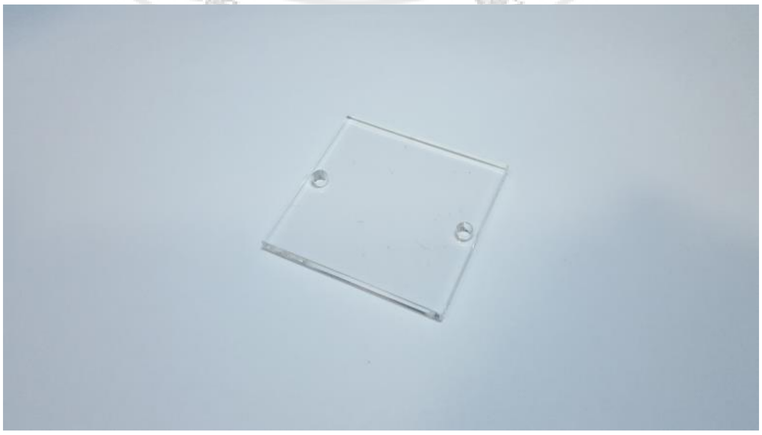

Figure 55: Syringe Outer Barrel Fixture Top

Figure 56: Syringe Push Rob Fixture

Figure 57: Screws, nuts and washers

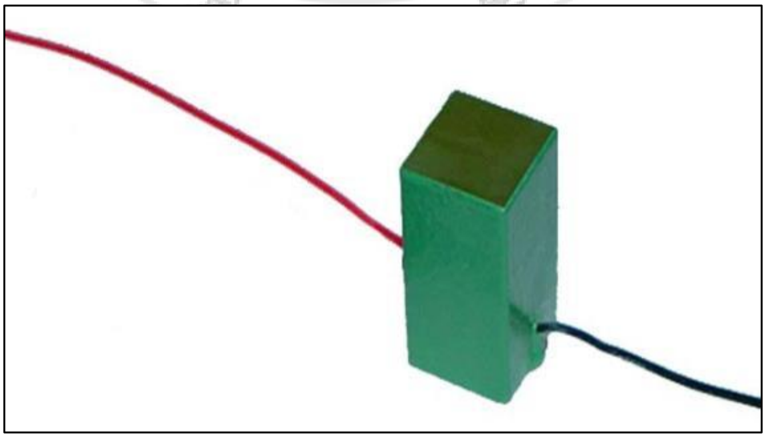

Figure 58: Piezoelectric Actuator

APPENDIX D: DEVICES USED IN EXPERIMENT

Hardware components are listed below:

1) Piezoelectric Actuator: TS18-H5-202, Piezo Systems, Inc.
2) Capacitive Sensor: D-510.050, Physik Instrumente (PI) GmbH & Co. KG
3) DAC: NI USB-6259, National Instruments Inc.
4) Signal Conditioner: E-852, Physik Instrumente (PI) GmbH & Co. KG
5) Microscope: SZ61, OLYMPUS CORPORATION
6) Voltage Amplifier: EPA-104-230, Piezo Systems, Inc.

APPENDIX E: PUBLICATION

1. In Nam Lei, Shihao Wen, Zeyi Wu, and Qingsong Xu, “Design and Testing of a Micro-Syringe Pump Driven by Piezoelectric Actuator,” in Proceedings of 2016 IEEE International Conference on Advanced Robotics and Mechatronics (ARM), Macau, China, August 18-20, 2016, (EI), (Submitted).

APPENDIX F: WORK BREAKDOWN